

# South–North and Radial Traverses through the Interplanetary Dust Cloud

E. Grün

*Max-Planck-Institut für Kernphysik, 69117 Heidelberg, Germany*  
E-mail: gruen@dusty.mpi-hd.mpg.de

P. Staubach

*ESA–ESOC, 64293 Darmstadt, Germany*

M. Baguhl

*Max-Planck-Institut für Kernphysik, 69117 Heidelberg, Germany*

D. P. Hamilton

*University of Maryland, College Park, Maryland 20742*

H. A. Zook

*NASA Johnson Space Center, Houston, Texas 77058*

S. Dermott and B. A. Gustafson

*University of Florida, Gainesville, Florida 32611*

H. Fechtig, J. Kissel, D. Linkert, G. Linkert, and R. Srama

*Max-Planck-Institut für Kernphysik, 69117 Heidelberg, Germany*

M. S. Hanner and C. Polanskey

*Jet Propulsion Laboratory, Pasadena, California 91103*

M. Horanyi

*Laboratory for Atmospheric and Space Physics, University of Colorado, Boulder, Colorado*

B. A. Lindblad

*Lund Observatory, 221 Lund, Sweden*

I. Mann

*Max-Planck-Institut für Aeronomie, 37191 Katlenburg-Lindau, Germany*

J. A. M. McDonnell

*University of Kent, Canterbury CT2 7NR, United Kingdom*

G. E. Morfill

*Max-Planck-Institut für Extraterrestrische Physik, 85748 Garching, Germany*

and

G. Schwehm

*ESA–ESTEC, 2200 AG Noordwijk, The Netherlands*

Received February 7, 1996; revised June 9, 1997

Identical *in situ* dust detectors are flown on board the Galileo and Ulysses spacecraft. They record impacts of micrometeoroids in the ecliptic plane at heliocentric distances from 0.7 to 5.4 AU and in a plane almost perpendicular to the ecliptic from  $-79^\circ$  to  $+79^\circ$  ecliptic latitude. The combination of both Ulysses and Galileo measurements yields information about the radial and latitudinal distributions of micron- and sub-micron-sized dust in the Solar System. Two types of dust particles were found to dominate the dust flux in interplanetary space. Interplanetary micrometeoroids covering a wide mass range from  $10^{-16}$  to  $10^{-6}$  g are recorded mostly inside 3 AU and at latitudes below  $30^\circ$ . Interstellar grains with masses between  $10^{-14}$  and  $10^{-12}$  g have been positively identified outside 3 AU near the ecliptic plane and outside 1.8 AU at high ecliptic latitudes ( $>50^\circ$ ). Interstellar grains move on hyperbolic trajectories through the planetary system and constitute the dominant dust flux ( $1.5 \times 10^{-4} \text{ m}^{-2} \text{ sec}^{-1}$ ) in the outer Solar System and at high ecliptic latitudes.

To compare and analyze the Galileo and Ulysses data sets, a new model is developed based on *J. Geophys. Res.* 98, 17029–17048, Divine's (1993, "five populations of interplanetary meteoroids" model. Both models describe the interplanetary meteoroid environment in terms of dust populations on distinct orbits. Taking into account the measured velocities and the effect of radiation pressure on small particles (described by the ratio of radiation pressure force to gravity,  $\beta$ ), we define four populations of meteoroids on elliptical orbits and one population on hyperbolic orbit that can fit the micrometeoroid flux observed by Galileo and Ulysses. Micrometeoroids with masses greater than  $10^{-10}$  g and negligible radiation pressure ( $\beta = 0$ ) orbit the Sun on low to moderately eccentric orbits and with low inclinations ( $\leq 30^\circ$ ). Populations of smaller particles with mean masses of  $10^{-11}$  g ( $\beta = 0.3$ ),  $10^{-13}$  g ( $\beta = 0.8$ ), and  $5 \times 10^{-15}$  g ( $\beta = 0.3$ ), respectively, have components with high eccentricities and have increasingly wider inclination distributions with decreasing mass. Similarities among the orbit distributions of the small particle populations on bound orbits suggest that all are genetically related and are part of an overall micrometeoroid complex that prevails in the inner Solar System. The high-eccentricity component of the small particle populations may actually be  $\beta$ -meteoroids which are not well characterized by our measurements. Our modeling suggests further that the interstellar dust flux is not reduced at Ulysses' perihelion distance (1.3 AU) and that it contributes about 30% of the total dust flux observed there. © 1997 Academic Press

## 1. INTRODUCTION

The traditional method to determine the global structure of the interplanetary dust cloud is by zodiacal light observations (for a recent review see, e.g., Leinert and Grün 1990). An inversion method allows investigators to derive the radial profile near 1 AU even from ground-based observations (Dumont and Levasseur-Regourd 1985). The vertical structure of the zodiacal cloud can also be inferred from

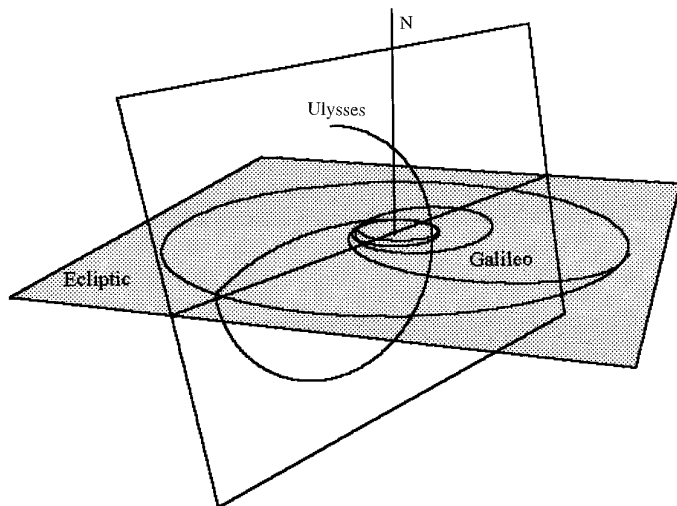


FIG. 1. Trajectories of Galileo and Ulysses. The Sun is in the center; Earth's, Jupiter's, and Galileo's trajectories are in the ecliptic plane (shaded). The initial trajectory of Ulysses from the Earth to Jupiter was also in the ecliptic plane. Subsequently Ulysses was thrown onto an orbit plane inclined  $79^\circ$  to the ecliptic.

ground-based zodiacal light measurements (Leinert *et al.* 1976, Levasseur-Regourd and Dumont 1980, Giese *et al.* 1986). Recent infrared observations by IRAS (Hauser *et al.* 1984) and especially COBE (Reach *et al.* 1995) give further constraints on the zodiacal dust cloud outside the Earth's orbit. The radial profile is obtained from spacecraft observations traversing the appropriate regions of space. Pioneer 10 and 11 (Hanner *et al.* 1976) and Helios observations (Leinert *et al.* 1981) covered interplanetary space between 0.3 and 18 AU, although zodiacal light was recognized only out to a distance of 3.3 AU from the Sun.

Here, we focus on another way to obtain information on the large-scale structure and the dynamics of the interplanetary dust cloud. *In situ* dust detectors onboard the Galileo and Ulysses spacecraft measure dust along their interplanetary trajectories. From these measurements a three-dimensional model of the interplanetary dust cloud is constructed. The orbits of the Galileo and Ulysses spacecraft are displayed in Fig. 1. After its launch on October 18, 1989, the massive Galileo spacecraft orbited the Sun twice and had a swing-by of Venus (February 10, 1990) and two swing-bys of the Earth (December 8, both 1990 and 1992) before it acquired enough orbital energy to reach Jupiter on December 7, 1995. The lightweight Ulysses spacecraft was launched (October 6, 1990) a year after Galileo onto a direct trajectory to Jupiter. After Jupiter flyby on February 8, 1992, the Ulysses spacecraft was thrown onto an orbit of  $79^\circ$  inclination that passed close to the ecliptic poles. The pass from the south to the north pole took 1 year from September 1994 to September 1995

and the passage through the ecliptic plane occurred on March 13, 1995.

Although the prime objective of the Galileo dust experiment (Grün *et al.* 1992c) is the measurement of dust near Jupiter, its 6-year orbit through the Solar System provided a unique opportunity to obtain unprecedented information on the dust populations near the ecliptic plane. The objectives of the Ulysses dust experiment (Grün *et al.* 1992b) were (1) to determine the three-dimensional structure of the zodiacal cloud, (2) to characterize its dynamical state, and (3) to search for interstellar dust penetrating the Solar System.

The achievement of the third Ulysses objective, namely, the identification of interstellar dust particles, complicates the achievement of the first two objectives because at every point in space interstellar dust has to be identified and separated from interplanetary dust. For measurements by both the Galileo and Ulysses detectors, this distinction is easy outside about 3 AU because the flux of interstellar dust grains dominated and differed significantly in both direction and speed from prograde interplanetary dust (Grün *et al.* 1993, 1994, Baguhl *et al.* 1995a,b). Outside 3 AU, the interplanetary dust flux was very low and was hardly recognizable; therefore, we restrict our analysis of characterizing the interplanetary dust population to distances inside 3 AU. Here, the distinction between interplanetary and interstellar dust is more complicated and we must employ modeling to achieve this goal. In essence, Ulysses data are very good at determining the absolute latitude dependence (and inclination dependence) of meteoroids just outside 1.3 AU. Measurements by Galileo near the ecliptic determine along with spacecraft motion and position the radial and eccentricity dependence for low-inclination orbits. Similarly, observations at high angles with respect to the ecliptic determine high-inclination orbits.

To describe the interplanetary meteoroid environment, several meteoroid models have been developed in past decades. The most comprehensive model so far is the “five populations of interplanetary meteoroids” model of Divine (1993) that synthesizes meteor data, zodiacal light observations, and some *in situ* measurements of interplanetary dust. The model describes dust concentrations and fluxes on the basis of meteoroid populations with distinct orbital characteristics. In this paper we modify the Divine model to make it applicable to the complete Galileo and Ulysses data sets. Divine employs purely gravitational (Keplerian) dynamics to derive impact rates. However, for micron-sized dust we add the effect of radiation pressure on the dynamics. Besides impact rates, the Galileo and Ulysses dust instruments provide important directional and speed information that can constrain models. We also add an interstellar dust population which penetrates the Solar System on hyperbolic trajectories.

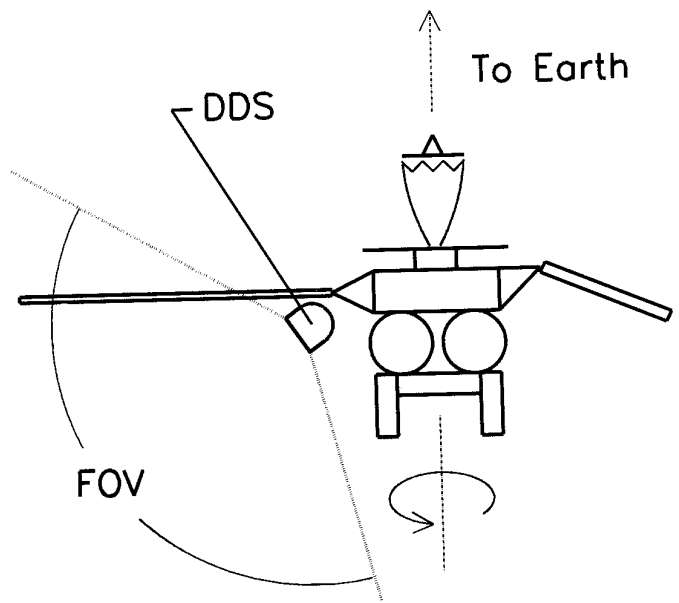


FIG. 2. Schematic view of the Galileo spacecraft, its antenna direction and spin axis orientation, and the mounting of the dust detector system (DDS) with the sensor axis and the field of view (FOV). The boom to which the dust detector is mounted has only little effect (<10%) on the FOV in the forward direction.

In the following section we describe the relevant instrumental characteristics before we describe in detail the Galileo and Ulysses dust measurements in Sections 3 and 4. In-ecliptic dust data were obtained primarily during Galileo’s flight through the Solar System out to about 3 AU, whereas the latitudinal data were obtained during Ulysses’ trajectory from the ecliptic south to the ecliptic north pole. In the fifth section, we derive dust fluxes that can be compared with a model. Important characteristics of the new dust model are described in Section 6. Section 7 discusses properties of the new interstellar and interplanetary dust populations. The vertical structure of the interplanetary dust cloud is explored in Section 8. In Section 9 model and measurements are compared and the results are discussed, and in the final section we summarize our findings.

## 2. INSTRUMENTATION

Both Galileo and Ulysses are spinning spacecraft with their antennas usually pointing close to the Earth; i.e., the spin axes are parallel to the spacecraft–Earth line. The primary exception was when the Galileo spacecraft was inside the Earth’s orbit; there its antenna was pointed toward the Sun. Both spin periods are about 20 sec. Figure 2 is a schematic view of the Galileo spacecraft (Johnson *et al.* 1992) which shows the mounting of the dust detector

system (DDS). The axis of the Galileo dust detector points  $125^\circ$  away from the antenna direction. On the much smaller Ulysses spacecraft (Wenzel *et al.* 1992) the dust detector is mounted at an angle of  $85^\circ$  from the antenna direction. In both cases the spin-averaged effective sensor area for impacts varies according to the angle,  $\gamma$ , between impact direction and the anti-antenna direction (Fig. 3) (cf. Grun *et al.* 1992b).

The field of view (FOV) of both dust detectors is a cone of full angle  $140^\circ$ . The impact direction (rotation angle) in a plane perpendicular to the spacecraft axis is determined by the spin position of the spacecraft at the time of impact. This angle gives the rotation of the spacecraft around its spin axis, where zero occurs when the dust sensor axis is closest to the ecliptic north direction. The rotation angle is measured in a right-handed system around the antenna direction.

Figure 4 displays scans of the sensor axis in an ecliptic spherical coordinate system during a single spin revolution (rotation angle  $0^\circ$  to  $360^\circ$ ) at different positions along the Galileo and Ulysses trajectories. For comparison the spacecraft-centered up-stream direction of the interstellar gas and dust flow is shown separately for each position. The direction of the interstellar flow direction is not fixed in this representation since the relative speed vector varies according to the actual spacecraft speed. The four Galileo positions (Fig. 4a) refer to the second orbit (between the two Earth flybys). Because the Galileo trajectory did not deviate much from the ecliptic plane the spin axis of the spacecraft stayed close to the ecliptic plane and the sensor axis scanned a latitude range about  $55^\circ$  on both sides of the ecliptic. During one orbit around the Sun the scan covered the full longitude range. The sensitivity of the scan for the interstellar flow direction varies during the course

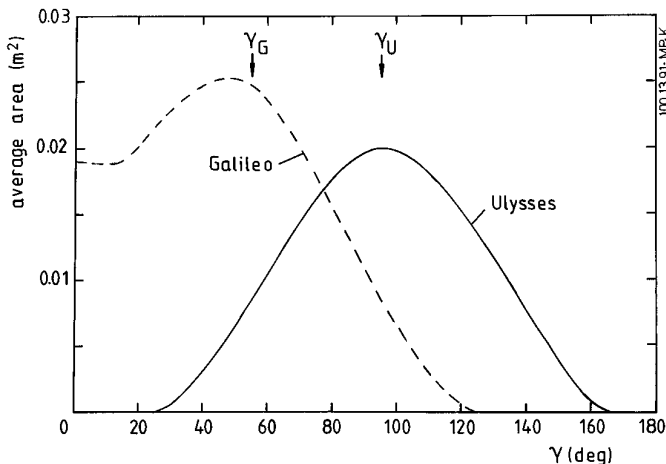


FIG. 3. Spin averaged angular sensitivities of the Galileo and Ulysses dust sensors as a function of the angle between the impact and anti-antenna directions.

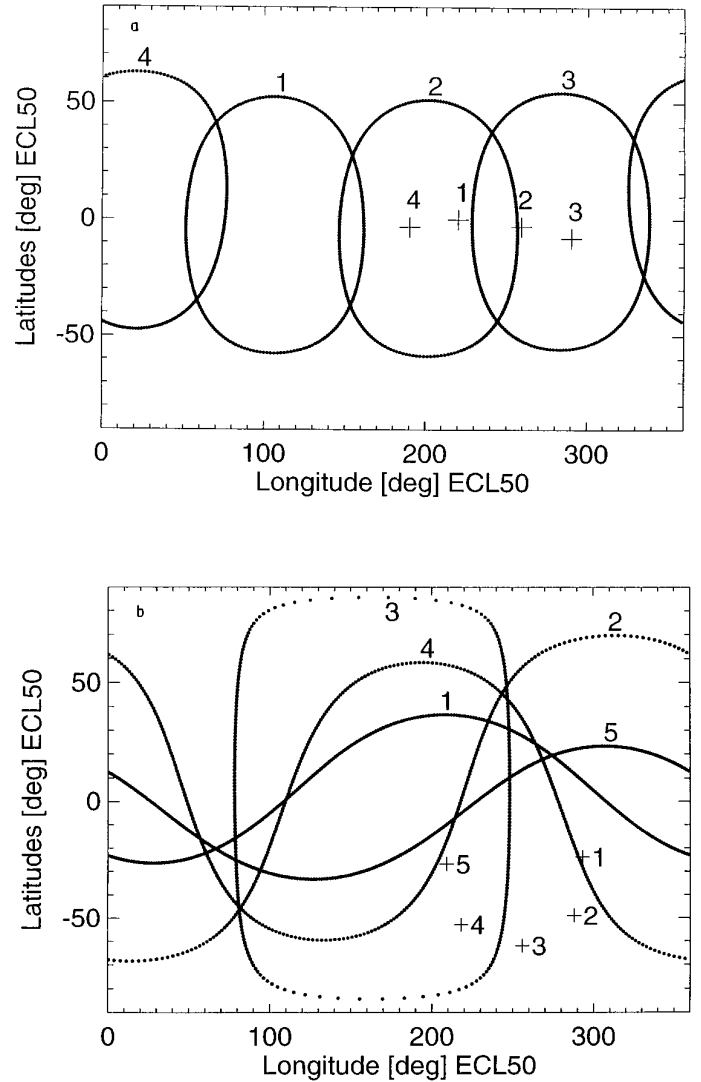


FIG. 4. Latitudes and longitudes (S/C centered ECL50 system) of the dust sensor axis at different spacecraft positions. Sensor pointing directions are shown for a full spin rotation (rotation angle  $0^\circ$  to  $360^\circ$ ). Rotation angle is measured from the direction closest to the ecliptic north direction in counterclockwise sense. Upstream directions of the interstellar gas and dust (crosses) are given for the different spacecraft positions. The actual FOV of the dust sensor is the area within  $70^\circ$  around the sensor axis direction. (a) Sensor pointing directions at four positions during Galileo's second orbit around the Sun, between E1 and E2 [approximately  $90^\circ$  in ecliptic longitude apart, (1) December 1990, (2) February 1991, (3) July 1991, (4) June 1992]. (b) Sensor pointing directions at five positions during Ulysses' traverse from the ecliptic south to the ecliptic north pole: (1)  $-79^\circ$ , (2)  $-45^\circ$ , (3)  $0^\circ$ , (4)  $+45^\circ$ , (5)  $+79^\circ$ . Crosses show the interstellar direction at corresponding times.

of an orbit around the Sun. At position 4, the interstellar grain flux direction is outside the Galileo sensor FOV for all rotation angles. Figure 4b displays scans of the Ulysses sensor for five positions on its trajectory from the south to the north pole. Near the poles ( $\pm 79^\circ$ ), the Ulysses sensor

axis scans only over small latitudinal excursions ( $<40^\circ$  off a plane parallel to the ecliptic), while during ecliptic plane crossings the scan covers the whole latitudinal range at two longitudes about  $170^\circ$  apart. Taking into account the  $70^\circ$  FOV of the detector, interstellar dust is observable at all positions.

The dust detectors aboard Galileo (Grün *et al.* 1992c) and Ulysses (Grün *et al.* 1992b) are identical impact ionization sensors that measure the plasma cloud generated on impact of submicron- and micron-sized dust particles onto the gold metal target of the detector. Several independent measurements of the ionization cloud created during impact are used to derive both mass and speed of the dust grains (Grün *et al.* 1995c). The dynamic range of the impact charge measurement is  $10^6$  which corresponds to the dynamic range of the mass determination. The uncertainty of a single mass determination is about a factor of 10. Impact speeds can be determined (in the calibrated range from 2 to 70 km/sec) with an accuracy of about a factor of 2.

The detector mass threshold,  $m_t$ , is proportional to the positive charge component,  $Q_1$ , of the plasma produced during the impact, which itself strongly depends on the impact speed. To compare early low-sensitivity Galileo dust data with Ulysses data we have to restrict our analysis to dust impacts that produce impact charges greater than  $8 \times 10^{-14}$  C, for which we have complete count rates even at Galileo's reduced data transmission rate (Baguhl *et al.* 1993). Using the calibration parameters  $(Q_1/m)_0$ ,  $m_0$ ,  $v_0$ , and  $\alpha$ , which have been approximated from detector calibrations (Grün *et al.* 1995c), the corresponding mass threshold can be calculated:

$$m_t = \frac{Q_1}{(Q_1/m)_0} = m_0 \left( \frac{v_0}{v} \right)^\alpha, \quad (1)$$

with  $\alpha \approx 3.5$ . For example, an impact charge of  $Q_1 = 8 \times 10^{-14}$  C refers to a mass threshold  $m_t = 3 \times 10^{-14}$  g at 20 km/sec impact speed. After reprogramming in mid-1994, the Galileo dust instrument reached the same sensitivity ( $10^{-14}$  C) as the Ulysses instrument, even at the very low data transmission rate supported by Galileo.

Impact-related data such as impact charge, impact time, and rotation angle are normally all transmitted to Earth for each impact. In addition, the occurrence of an impact advances an 8-bit counter whose value is also transmitted. However, because Galileo relies on its low-gain antenna for data transfer (its high-gain antenna failed to deploy), it cannot always transmit data in real time and must store data onboard. Because of limited data storage capability within the instrument, some dust data are overwritten before they can be transmitted; i.e., the information from which the mass, velocity, and impact direction can be de-

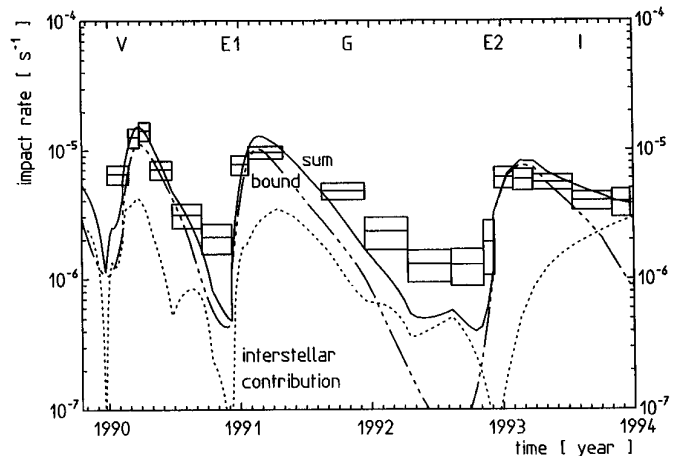


FIG. 5. Galileo impact rate during the first 4 years of the mission. The boxes indicate the mean impact rate and the standard deviation. V, E1, E2, G, and I are flybys of Venus (February 10, 1990), Earth (E1, December 8, 1990; E2, December 8, 1992), and the asteroids Gaspra (G, October 29, 1991) and Ida (I, August 28, 1993). Shortly after Venus flyby Galileo reached perihelion of 0.7 AU; aphelion of the first orbit about the Sun was between V and E1 at 1.28 AU. Aphelion of the second orbit was between G and E2 at 2.23 AU. At the end of 1993 Galileo had reached a distance of 3.7 AU. No data have been recorded by the dust detector during the gap of the impact rates between E1 and G. Model calculations of the impact rate during the first 4 years of the Galileo mission are shown. Both individual contributions from interplanetary dust on *bound* orbits and *interstellar* dust on hyperbolic trajectories and the *sum* of both are displayed.

rived is lost. Even for impacts for which detailed data are overwritten, however, the fact that one or more such impacts occurred is stored in the counter and is transmitted to Earth. Thus, we have two types of data: (i) individual impacts for which we have a complete record of impact charge, particle mass, relative velocity, impact time, and impact direction, and (ii) impact rates derived from accumulated data. The former correspond only to a small subset of all impacts recorded on board, while the latter is a complete record of all impacts.

### 3. IN-ECLIPTIC MEASUREMENTS BY GALILEO

From launch in 1989 until September 1993, the orbit of the Galileo spacecraft was within 3 AU of the Sun and close ( $<5^\circ$ ) to the ecliptic plane, i.e., in the region where interplanetary dust should be most prominent. Dust streams from Jupiter had not yet been detected by Galileo (Grün *et al.* 1996). The impact rate observed by Galileo during the first 4 years in orbit is shown in Fig. 5. The impact rate varied strongly with time due to varying heliocentric distance and varying spacecraft motion with respect to the viewing direction of the dust sensor; i.e., the rate was high when the spacecraft moved away from the Sun in the direction the dust sensor was facing. Orbit changes due to flybys of Venus and the

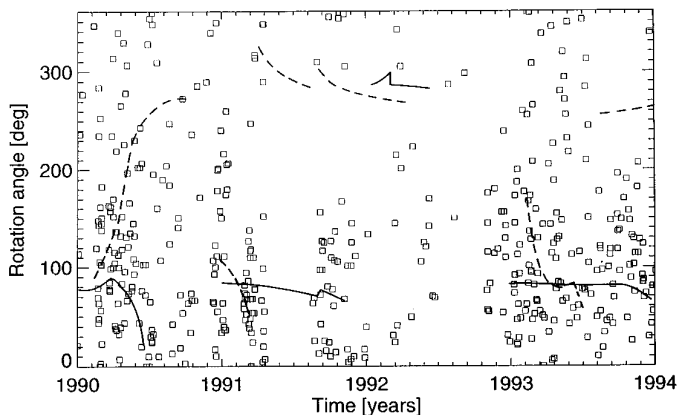


FIG. 6. Rotation angle of dust impacts during the first 4 years of the Galileo mission. Individual impacts with impact charge  $>8 \times 10^{-14}$  C are marked by squares. Solid lines show the center direction ( $\pm 70^\circ$ ) from which interstellar grains would arrive. Dashed lines represent the center direction from which particles on minimum-inclination, circular prograde orbits would arrive. These lines are shown only if the direction is visible by the detector for longer than a month.

Earth (twice) also had immediate effects on the impact rate. Flybys of the asteroids Gaspra and Ida did not produce any change in the impact rate, in agreement with the predictions of Hamilton and Burns (1992).

In Fig. 6 the spacecraft rotation angles of each of the 437 impacts are displayed for which we have complete information during the first 4 years of the mission. For most of the time, impacts were observed over the whole range of rotation angles. It should be noted that the presentation does not contain all impacts recorded by the dust instrument during this time: For some time intervals (total of 177 days) the instrument was not operational (Grün *et al.* 1995a), for some other periods no spin information was available on board the spacecraft (82 impacts), and, finally, for 20 impacts the complete information is unavailable on the ground and they were only counted. Nevertheless, it will be assumed that the missed impacts (about 30% of the recorded impacts) had the same rotation angle distribution as the other impacts.

Masses of 519 impacts are shown in Fig. 7. For most of the time the whole mass range from  $10^{-15}$  to  $10^{-6}$  g is covered. In the outer portions of the orbit (mid-1991 to end of 1992 and near the end of 1993) both the biggest and the smallest particles seem to be missing. The mass distribution of all the particles is shown in Fig. 8. Three-quarters of the particles have masses between  $10^{-13}$  and  $10^{-9}$  g; 12% each have masses smaller and bigger, respectively.

#### 4. OUT-OF-ECLIPTIC MEASUREMENTS BY ULYSSES

The Ulysses mission is especially well suited to obtain a latitudinal profile of the interplanetary dust cloud. In the

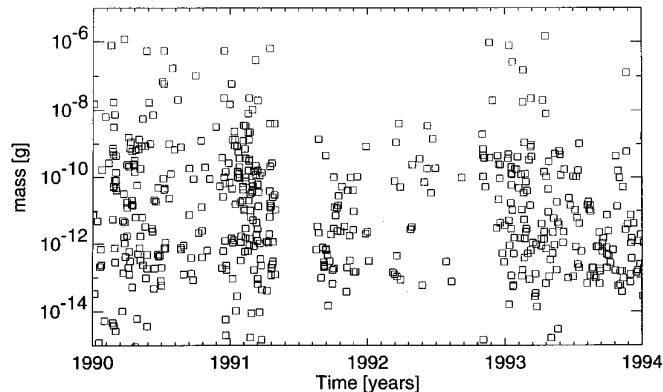


FIG. 7. Masses of dust particles observed during the first 4 years of the Galileo mission (impact charge  $>8 \times 10^{-14}$  C). The uncertainty of a mass determination is about a factor of 10. Periods of missing data are visible in 1991.

limited distance range from 2.3 to 1.3 AU, Ulysses passed from close to the ecliptic south pole ( $-79^\circ$  ecliptic latitude) through the ecliptic plane to the north pole ( $+79^\circ$ ). The outer portions of the out-of-ecliptic orbit (beyond 2.3 AU) are not suited for characterizing interplanetary dust because of the dominant interstellar dust population (Baguhl *et al.* 1995a). Over the solar south pole Ulysses discovered a population of small dust particles (Baguhl *et al.* 1995b) that are interpreted to be  $\beta$ -meteoroids affected by the solar wind magnetic field (Hamilton *et al.* 1996). These small particles of presumed interplanetary origin are not considered here because of our restriction to impact charges  $>8 \times 10^{-14}$  C.

The relation between the dust density at a given latitude and the inclination distribution is simply given by the fact that dust particles recorded at ecliptic latitude  $\lambda$  have to

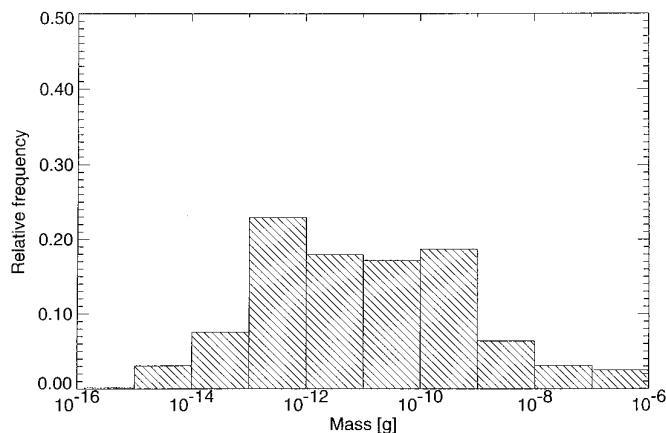


FIG. 8. Mass distribution of dust particles observed during the first 4 years of the Galileo mission.

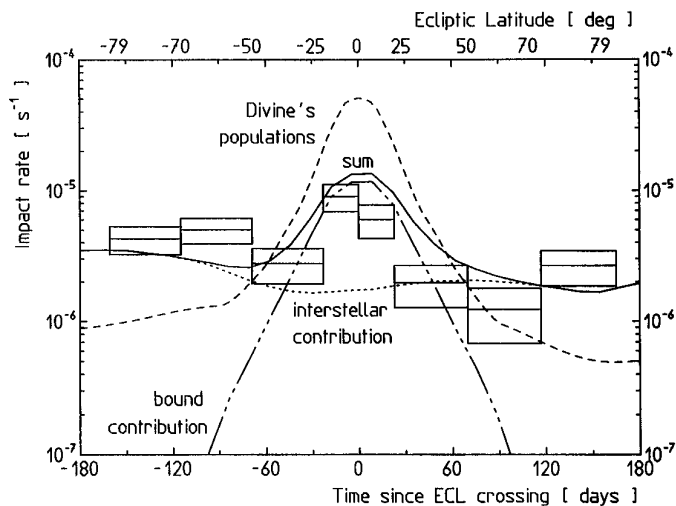


FIG. 9. Ulysses impact rate (impact charge  $>8 \times 10^{-14}$  C) observed around the time of its ecliptic plane crossing (ECL). ECL occurred on 12 March 1995 at a distance of 1.3 AU from the Sun. The boxes indicate the mean impact rate and the standard deviation. During all the time Ulysses was inside 2.3-AU distance from the Sun. The top scale gives the spacecraft latitude. Model calculations of the impact rate during Ulysses' south–north traverse through the ecliptic plane are shown by the lines. Both individual contributions from interplanetary dust on *bound* orbits and *interstellar* dust on hyperbolic trajectories and the *sum* of both are displayed. It has been assumed that interstellar dust is not depleted down to 1.3 AU. In comparison the prediction from the Divine (1993) model is shown.

have inclinations  $i \geq \lambda$  reach this latitude. Figure 9 shows the impact rate during the pole-to-pole traverse. The passages over the south and north poles occurred 170 days before and after ecliptic plane crossing, respectively. A total of 109 (with impact charges  $> 8 \times 10^{-14}$  C) were recorded during this time. The impact rate stayed relatively flat except for the maximum ( $9 \times 10^{-6}$  sec $^{-1}$ ) during ecliptic plane crossing. The impact rate at the northern leg is about a factor of 2 below that of the southern one. This is due to the varying spacecraft attitude which followed the direction to the Earth. This variation of spacecraft attitude is also reflected in the variations of rotation angles of the impacts which were detected during the south–north traverse (Fig. 10). Over the south pole most large impacts (with impact charges  $> 8 \times 10^{-14}$  C) occurred at rotation angles between  $0^\circ$  and  $150^\circ$  which includes the interstellar direction. Closer to the ecliptic plane the rotation angle range of large impacts widened and moved further to the north direction (rotation angle =  $0^\circ$ ). At ecliptic plane passage these impacts were recorded in a wide range around the north direction ( $0^\circ$  to  $100^\circ$  and  $200^\circ$  to  $360^\circ$ ). On the northern pass, rotation angles covered the whole range and above the north pole it ranged from  $50^\circ$  to  $200^\circ$ , again including the interstellar direction.

Figure 11 shows the masses of dust particles detected during the south–north traverse. Twenty particles with

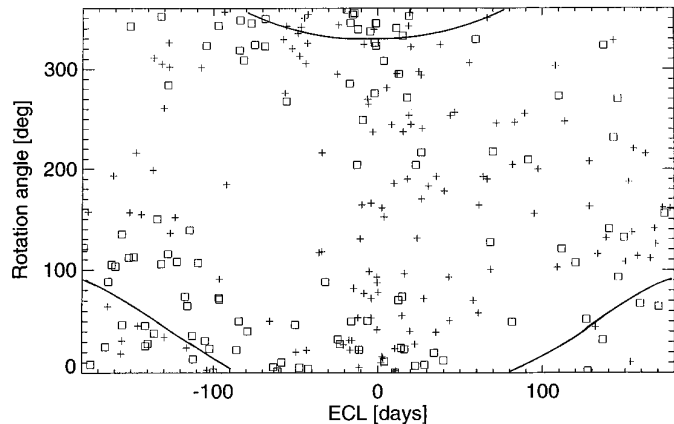


FIG. 10. Rotation angle of dust impacts as a function time from ecliptic plane crossing (ECL) of Ulysses. Individual impacts (squares, impact charge  $>8 \times 10^{-14}$  C; crosses,  $\leq 8 \times 10^{-14}$  C). The solid line shows the direction from which interstellar grains are expected. The direction from which particles on minimum-inclination ( $\leq 30^\circ$ ), circular prograde orbits would arrive coincides with the interstellar direction from ECL  $-40$  to ECL  $+40$  days.

masses greater than  $10^{-10}$  g were detected during the north–south traverse; 15 of these particles were recorded during the 80 days when the spacecraft was within  $30^\circ$  of the ecliptic plane. This increased flux of big particles near the ecliptic is obviously due to an interplanetary dust population.

In Fig. 12 mass distributions of particles recorded during the complete south–north traverse and during the pass from  $-30^\circ$  to  $+30^\circ$  ecliptic latitude are compared with the mass distribution of interstellar dust observed during about 2 years prior to the south pole passage; the corresponding impact rates are  $3.4 \times 10^{-6}$ ,  $5.4 \times 10^{-6}$ , and  $2.4 \times 10^{-6}$  sec $^{-1}$ , respectively. The total mass distribution during the

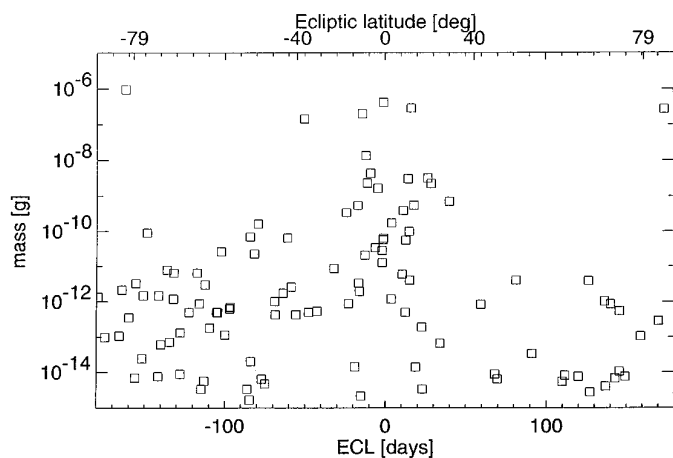


FIG. 11. Masses of dust particles observed during ecliptic plane crossing of Ulysses (impact charge  $>8 \times 10^{-14}$  C).

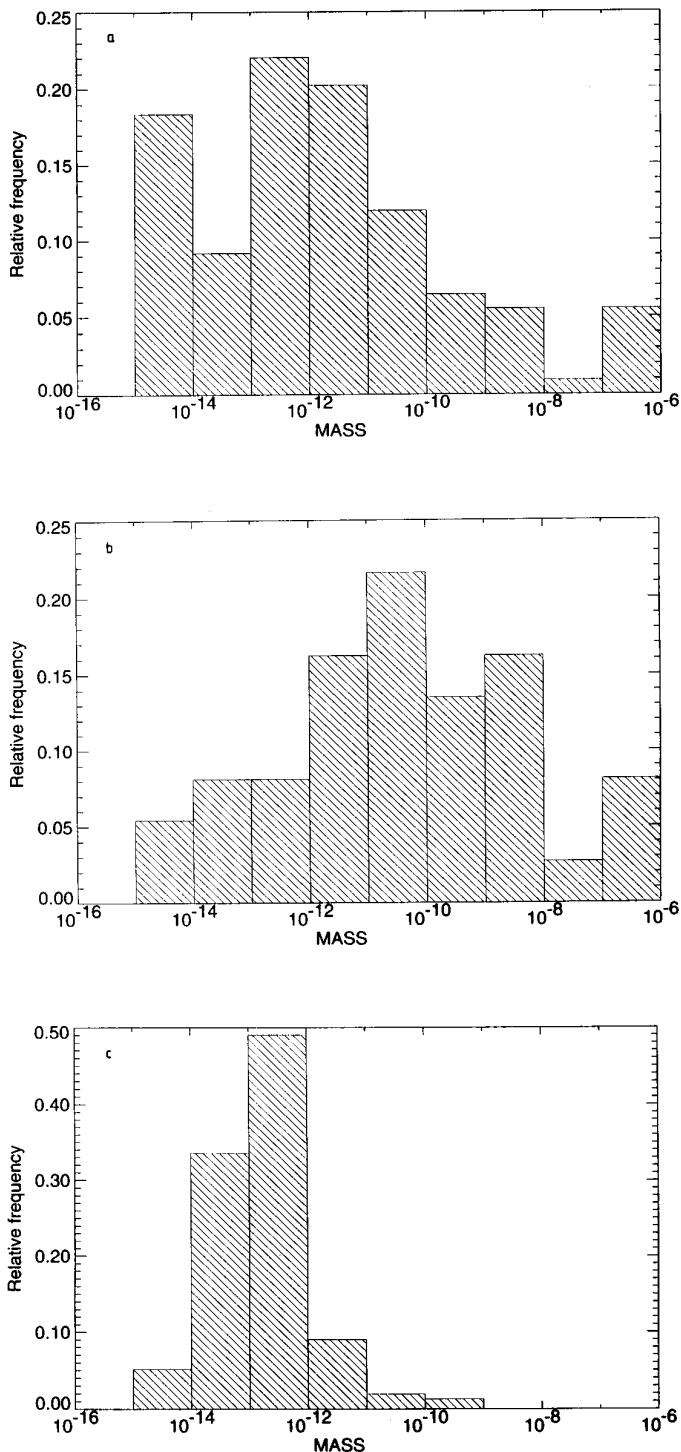


FIG. 12. Mass distributions of dust particles observed by Ulysses: (a) during the entire south–north traverse (360 days around ecliptic plane crossing, 109 impacts); (b) from  $-30^\circ$  to  $+30^\circ$  latitude (80 days, 37 impacts); (c) interstellar dust (from Jupiter to the south ecliptic pole, about 840 days, 155 impacts).

south–north traverse seems to be composed of two distinct components: the interstellar dust component, which has peak masses between  $10^{-14}$  and  $10^{-12}$  g and a bigger interplanetary dust component dominating the near-ecliptic region.

Ulysses traversed the interplanetary dust cloud rather rapidly and unfortunately the number of detected interplanetary particles is too small for a unique characterization of this population. Therefore, we use the Galileo data to further constrain interplanetary particles. The initial in-ecliptic portion of the Ulysses trajectory is also not well suited to give significant information on the interplanetary dust population because of its low sensitivity to low-inclination and low-eccentricity orbits (Grün *et al.* 1992a, Mann *et al.* 1996).

## 5. DIFFERENTIAL IMPACT RATES

As we have seen, the Galileo and Ulysses dust detectors provide speed and directional information in addition to total impact rates. This combined information will be used to constrain our model of the interplanetary dust cloud. In an earlier model Divine (1993) only used total impact rates from the initial phases of Galileo and Ulysses missions.

To compare the measured data with a model, all spacecraft-sensed impacts were analyzed and sorted into bins of time, speed, and impact direction. Each data set is divided into periods according to the significant points on the trajectory (planetary flybys). Each period is then divided into several time intervals containing about the same number of impacts. In Table I the time intervals and the corresponding portions of the spacecraft trajectories are specified for which differential impact rates have been determined.

The impact velocity in the calibrated range (2 to 70 km/sec) is divided into three intervals ( $<10$ , 10 to 25, and  $>25$  km/sec). The impact direction (rotation angle) is divided into four equal intervals of  $90^\circ$ . To minimize statistical problems (because of the large number of bins in comparison to the number of impacts) an averaging algorithm has been developed to sort all particles into these bins (Staubach 1996a, Staubach *et al.* 1996). The full ranges of times, velocities, and rotation angles correspond to a cube of unit volume (cf. Fig. 13). Each particle impact is represented by a point in three-dimensional time–velocity–rotation space. Each impact point is used as center of a sphere. The radii of the spheres are chosen in such a manner that only a selected number of impacts are contained in the sphere. Best results have been obtained using numbers of four or five particle impacts. Using a lower number the averaging gets worse, while for higher numbers the loss of information increases because of the smoothing process. In the following the mean of the two radii (con-

**TABLE I**  
**Time Intervals and Spatial Boundaries of Galileo and Ulysses Flux Data**

Bin	Time interval (year–day)		Distance (AU)		Latitude (deg)	
	Begin	End	Min	Max	Min	Max
a. Galileo flux data						
G1	89–362	90–41	0.72	0.98	3.3	3.6
G2	90–41	90–121	0.72	0.95	–1.5	3.3
G3	90–121	90–342	0.95	0.99	–1.5	0.0
G4	90–342	91–56	0.99	1.04	–4.5	0.0
G5	91–56	91–249	1.04	2.07	–4.5	1.1
G6	91–249	92–342	0.99	2.07	0.1	1.1
G7	92–342	93–144	0.99	2.20	–1.3	0.1
G8	93–144	94–12	2.20	3.79	–1.3	–0.7
G9	94–12	94–257	3.79	4.77	–0.7	–0.3
G10	94–257	95–149	4.77	5.25	–0.3	0.0
b. Ulysses flux data						
U1	90–300	91–206	1.02	3.72	0.9	1.5
U2	91–206	92–39	3.72	5.40	1.1	1.5
U3	92–39	93–102	4.82	5.40	–21.5	1.1
U4	93–102	94–113	3.23	4.82	–53.7	–21.5
U5	94–113	95–24	1.44	3.23	–79.4	–36.3
U6	95–24	95–270	1.30	2.43	–36.3	75.3

taining four and five impacts) have been used. To simplify further evaluations, each sphere is transformed into a cube with identical volume. Finally, fractions of the number of particles (in the cube) have been distributed into the bins according to their common volume. For further analysis each bin is given a weight corresponding to the number of impacts contained.

Table II gives the measured and smoothed differential impact rates of Galileo and Ulysses for all time, speed, and rotation angle bins. Interstellar particles are observed mainly at rotation angles of about  $90^\circ$ . Since these particles are the dominant populations in the outer Solar System, they cause the highest fluxes in the first rotation angle bin ( $45^\circ$ – $135^\circ$ ) and at the highest velocities. A significantly lower flux occurs in the third rotation bin ( $225^\circ$ – $315^\circ$ ), especially at high velocities, because only few interplanetary particles (on prograde orbits) were measured and their flux was low. In the inner Solar System, slow particles on prograde, heliocentric bound orbits are the dominant population observed by Galileo.

## 6. THE MICROMETEOROID MODEL

For the model description of micrometeoroids we follow in principle the method of Divine (1993) with the following modifications: we include the effect of radiation pressure

on the velocity of micrometeoroids and we consider impact directions and speeds. The goal of our dynamical modeling is to describe the spatial density of dust and the directional flux at each position in space by a “model” distribution of orbital elements and compare the resulting fluxes with the measured values. Following Divine (1993) the interplanetary meteoroid complex is represented by several populations of dust particles that are defined by their orbital element and mass distributions. To simplify the meteoroid model, several assumptions are made: (1) the dust cloud is symmetric about the ecliptic plane, and (2) it has rotational symmetry, i.e., the longitudes of nodes and arguments of perihelion of dust orbits are uniformly distributed. Therefore, in our model the spatial dust density depends only on distance  $r$  from the Sun and height  $z$  above the ecliptic plane. Small asymmetries relative to the ecliptic plane (cf. Leinert and Grün 1990) or an offset of the cloud center from the Sun (Dermott *et al.* 1994) are ignored. No time dependencies are considered, although for the submicron dust flux a 22-year cycle has been suggested (Morfill and Grün 1979, Gustafson and Misconi 1979, Hamilton *et al.* 1996).

The ratio of radiation pressure force  $F_{\text{rad}}$  to gravitational attraction by the Sun,  $F_{\text{grav}}$ , is defined by the factor  $\beta = F_{\text{rad}}/F_{\text{grav}}$  (Burns *et al.* 1979). This  $\beta$  value is strongly dependent on material composition and structure of the

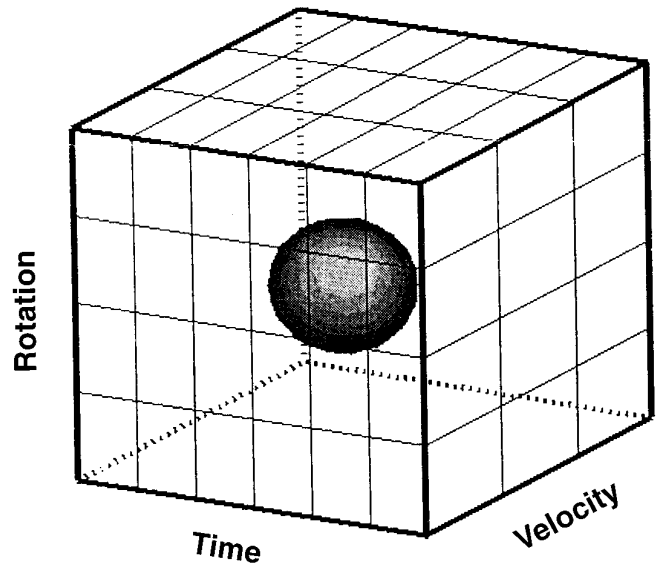


**FIG. 13.** Diagram showing the binning process: the unit cube representing the full ranges of time, speed, and rotation angle is divided into bins (Galileo: 10 time bins, Ulysses: 6 time bins, 3 speed bins, and 4 impact direction bins). Each impact is in the center of a sphere inside the large cube. Each sphere is just big enough to contain four or five neighboring impacts. Portions of the volumes of the spheres are then allocated to the bins of the cube.

TABLE II

Logarithm of the Measured Average Differential Fluxes in the Time, Speed, and Rotation Angle Intervals for Galileo and Ulysses

Time bin	Speed bin (km/sec)	Rotation angle bin			
		45°–134°	135°–225°	225°–315°	315°–45°
a. Galileo					
G1	< 10	-5.04	-5.12	-5.32	-5.33
	10–25	-5.53	-5.65	-5.93	-5.90
	>25	-5.10	-5.54	-6.24	-5.64
G2	<10	-4.71	-4.87	-5.12	-4.96
	10–25	-5.09	-5.40	-5.78	-5.49
	>25	-4.99	-5.37	-6.16	-5.64
G3	<10	-5.12	-5.30	-5.47	-5.15
	10–25	-5.30	-5.57	-5.99	-5.54
	>25	-5.51	-5.76	-6.11	-5.89
G4	<10	-4.65	-5.03	-5.38	-4.89
	10–25	-5.03	-5.82	-5.84	-5.23
	>25	-5.25	-5.96	-6.10	-5.70
G5	<10	-4.96	-5.36	-5.61	-5.16
	10–25	-4.83	-5.62	-5.84	-5.11
	>25	-5.06	-5.68	-5.85	-5.22
G6	<10	-5.48	-5.72	-6.35	-5.80
	10–25	-5.75	-6.14	-6.40	-5.70
	>25	-6.12	-6.45	-6.79	-6.11
G7	<10	-5.05	-5.15	-5.41	-5.34
	10–25	-5.23	-5.42	-6.10	-5.62
	>25	-5.28	-5.85	-6.92	-5.90
G8	<10	-5.57	-5.63	-5.89	-5.70
	10–25	-5.07	-5.70	-6.42	-5.69
	>25	-5.24	-5.88	-6.82	-5.88
G9	<10	-5.57	-5.70	-6.04	-5.68
	10–25	-5.11	-5.54	-6.41	-5.78
	>25	-5.34	-5.92	-6.71	-5.91
G10	<10	-5.69	-5.78	-6.03	-5.74
	10–25	-5.20	-5.49	-6.20	-5.68
	>25	-5.55	-5.93	-6.29	-5.78
b. Ulysses					
U1	<10	-5.87	-6.07	-6.39	-6.05
	10–25	-5.31	-5.97	-6.51	-6.10
	>25	-5.28	-5.76	-6.04	-5.85
U2	<10	-5.86	-6.18	-6.72	-6.18
	10–25	-5.18	-5.86	-6.71	-5.75
	>25	-5.19	-5.86	-6.95	-5.91
U3	<10	-6.31	-6.01	-6.59	-6.79
	10–25	-5.24	-5.62	-6.81	-6.14
	>25	-5.09	-5.57	-6.96	-6.23
U4	<10	-6.08	-6.18	-7.28	-6.72
	10–25	-5.41	-6.06	-6.85	-6.05
	>25	-5.22	-6.05	-6.54	-5.81
U5	<10	-5.65	-6.08	-6.18	-5.88
	10–25	-5.43	-6.44	-6.07	-5.44
	>25	-5.41	-6.00	-5.91	-5.34
U6	<10	-5.90	-6.21	-5.96	-5.48
	10–25	-5.60	-6.54	-6.11	-5.37
	>25	-5.84	-5.92	-5.83	-5.53

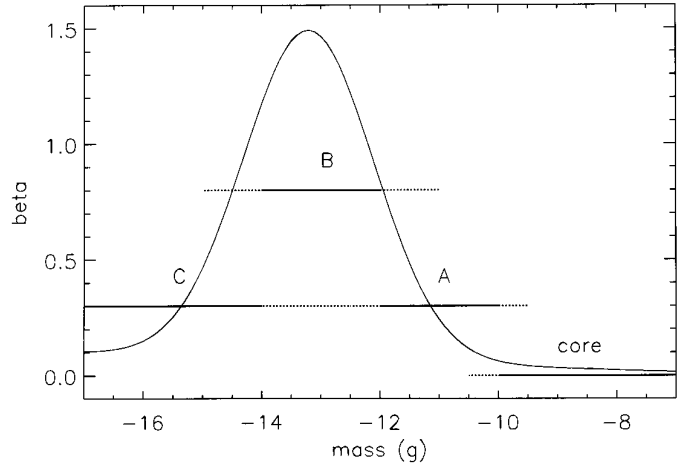


FIG. 14.  $\beta$ -values (force ratio of radiation pressure and gravity, from Gustafson 1994) assumed in the model as function of particle mass. Mass ranges and corresponding  $\beta$  values for dust populations on bound orbits ( $\beta < 1$ ) are indicated by solid lines (main contribution) and dashed lines (weak contributions).

dust particles. In this study, values obtained by Gustafson (1994) from Mie calculations for homogeneous spheres are taken. For particles with masses greater than  $10^{-10}$  g the influence of radiation pressure is negligible. At  $10^{-11}$ ,  $10^{-13}$ , and  $5 \times 10^{-15}$  g,  $\beta$  values of 0.3, 0.8, and 0.3, respectively, have been assumed. For bound orbits  $\beta < 1$  is required. Figure 14 shows the mass ranges and the corresponding  $\beta$  values considered here. These values correspond roughly to slightly absorbing dielectric particles (astronomical silicates, Draine and Lee 1984).

To evaluate the flux at position  $\mathbf{r}$  (bold characters indicate vector quantities) the relative velocity has to be determined from the orbital elements perihelion distance,  $r_1$ , eccentricity,  $e$ , and inclination,  $i$ , and from the  $\beta$  value. First, we give the velocity components in spherical coordinates, using intermediate quantities  $\lambda = \sin^{-1}(z/r)$ ,  $\chi = \sin^{-1}(r_1/r)$  and  $e_\chi = (1 - \sin \chi)/(1 + \sin \chi)$ :

$$\begin{aligned}
 v_r &= \pm \left[ \frac{GM_0(1-\beta)}{r^2 r_1} (r - r_1) \{ (1+e)r_1 - (1-e)r \} \right]^{1/2} \\
 &= \pm \left[ \frac{GM_0(1-\beta)}{r} \frac{(\cos \chi)^2}{\sin \chi} (e - e_\chi) \right]^{1/2}, \quad (3)
 \end{aligned}$$

$$v_\varphi = [\{GM_0(1-\beta)/r\}(1+e) \sin \chi]^{1/2},$$

$$v_\lambda = \pm v_\varphi [(\cos \lambda)^2 - (\cos i)^2]^{1/2}.$$

Because of the chosen symmetries there are two solutions for  $v_r$  and  $v_\lambda$  at a given point that correspond to inward, outward, upward, and downward directed velocities. With

these definitions the velocity components in Cartesian ecliptic coordinates are derived (cf. Divine 1993):

$$\begin{aligned} v_x &= \frac{x}{r} v_r - \left[ \frac{ryv_\varphi(\cos i) + xzv_\lambda}{x^2 + y^2} \right], \\ v_y &= \frac{y}{r} v_r - \left[ \frac{rxv_\varphi(\cos i) + yzv_\lambda}{x^2 + y^2} \right], \\ v_z &= \frac{z}{r} v_r + v_\lambda. \end{aligned} \quad (4)$$

Hence, the relative velocity  $\mathbf{u}_D$  between a particle with velocity  $\mathbf{v}$  and the spacecraft with velocity  $\mathbf{v}_{DB}$  is simply  $\mathbf{u}_D = \mathbf{v} - \mathbf{v}_{DB}$ . The sensitivity of a detector can be expressed by its mass threshold  $m_t$  and its angular sensitivity. For Galileo and Ulysses the effective sensitive area,  $\Gamma$ , is a function of the angle,  $\gamma$ , between the impact direction and the spacecraft axis. Let  $\mathbf{r}_D$  be a unit vector that specifies the spacecraft orientation (i.e., anti-antenna direction); the angle  $\gamma$  between  $\mathbf{r}_D$  and the direction from which the particle arrives is

$$\gamma = \arccos(-\mathbf{u}_D \cdot \mathbf{r}_D / |\mathbf{u}_D|). \quad (5)$$

The effective sensitive area  $\Gamma$  as a function of  $\gamma$  is shown in Fig. 3.

Populations of interplanetary meteoroids are described by independent distributions of orbital inclination  $p_i(i)$ , eccentricity  $p_e(e)$ , perihelion distance  $N_1(r_1)$ , and particles mass  $H_M(m)$ , and the corresponding  $\beta$  values. A discussion of these distribution functions is given by Matney and Kessler (1996). The cumulative mass distribution  $H_M(m_i)$  describes the ratio of the total mass in the distribution to the number of particles whose mass exceeds  $H_M(m_i) = \int_{m_i}^{\infty} dm \cdot H_m$ . The detector threshold  $m_t$ , angular sensitivity  $\Gamma$ , and a scale factor  $F_s$  to express the flux in different units and  $H_M(m_i)$  are ingredients in the dimensionless weighting function  $\eta_D$ :

$$\eta_D = F_s \Gamma H_M(m_i). \quad (6)$$

Together with the auxiliary variables  $\chi$  and  $e_\chi$  (defined above) the meteoroid flux  $J_{mt}$  can be calculated:

$$\begin{aligned} J_{m,t} &= \frac{1}{4\pi} \sum_{l=1}^4 \int_0^{\pi/2} d\chi \cdot N_1 \cdot \sin \chi \cdot \int_{e_\chi}^1 de \frac{p_e}{\sqrt{e - e_\chi}} \\ &\cdot \int_{|\lambda|}^{\pi-|\lambda|} di \frac{p_i \sin i}{\sqrt{\cos^2 \lambda - \cos^2 i}} \cdot (\eta_D \cdot \nu_D)_l. \end{aligned} \quad (7)$$

The summation over  $l$  corresponds to the four cases for the relative velocity: in/out and up/down (cf. Divine, 1993).

The flux in a given rotation angle interval ( $\rho_{\min}$  to  $\rho_{\max}$ ) and speed interval ( $v_{\min}$  to  $v_{\max}$ ) is obtained by integrating over only a limited  $\nu_D$  range (where  $v_R$ ,  $v_\rho$ ,  $v_\gamma$  are the velocity components in a spacecraft-fixed spherical coordinate system with the anti-antenna direction at  $\gamma = 0$ ):  $v_R$  from  $v_{\min}$  to  $v_{\max}$ , and  $v_\rho$  from  $\rho_{\min}$  to  $\rho_{\max}$ .

For any assumed dust population [defined by its distribution functions  $N_1(r_1)$ ,  $p_i(i)$ ,  $p_e(e)$ ,  $H_M(m)$ , and corresponding  $\beta$  value] and a given observation condition (spacecraft position,  $\mathbf{r}_{DB}$ , velocity,  $\mathbf{v}_{DB}$ , orientation,  $\mathbf{r}_D$ , and sensitivity weighting factor,  $\eta_D$ ), model fluxes can be calculated and compared with the corresponding measurement. The difference between the measurement and the sum of model fluxes of all dust populations is expressed by a mean and a root-mean-square (RMS) residual. Each distribution function consists of a distinct number of parameters which were varied by an iteration algorithm in such a way that the RMS residual was minimized. To enable a reasonable computation time the number of parameters needed to describe the distribution was chosen to be as low as possible (5 to 10). Since the iteration algorithm can find only a local minimum of the RMS residual the robustness of the results was tested by shifting individual distribution parameters in arbitrary directions and checking their return to the same solution. It should be noted that each parameter has a different influence on the residual, and, therefore, parameters having the strongest influence are defined most precisely.

## 7. POPULATIONS OF MICROMETEOROIDS

Although Galileo and Ulysses dust data cover a mass range from  $10^{-16}$  to  $10^{-6}$  g, the statistically best and most complete measurements range from  $10^{-14}$  to  $10^{-9}$  g. Because of the speed-dependent sensitivity threshold [Eq. (1)] several biases are introduced: (1) only particles that have masses in excess of the threshold mass are detected, and (2) saturation effects of the detector limit the useful mass range for big particles. Therefore, the mass distribution cannot be fully determined over a wide range of masses by a single *in situ* dust detector. The mass distribution of the interplanetary dust flux is best known near the Earth. It has been determined from lunar crater counts and Earth-orbiting spacecraft (Pegasus, Explorer 16 and 23, Pioneer 8 and 9, LDEF, and many other spacecraft). We use here the mass distribution  $H_m$  that Divine (1993) derived from the measurements presented by Grün *et al.* (1985). In addition, we use the radial dependence of the dust density that is based on zodiacal light observations by Helios (Leinert *et al.* 1981).

We first define the interstellar dust population, which is well represented by Galileo and Ulysses dust measurements at large heliocentric distances. Interstellar dust in interplanetary space was initially identified by the dust detector on board Ulysses after Jupiter flyby (Grün *et al.*

1993, 1994). Covering ecliptic latitudes between  $0^\circ$  and  $54^\circ$  and heliocentric distances between 5.4 and 3.2 AU, the flux of interstellar particles with a mean mass of  $3 \times 10^{-13}$  g stayed nearly constant at a flux value of about  $1.5 \times 10^{-14}$   $\text{m}^{-2} \text{sec}^{-1}$ . The presence of interstellar dust in the outer Solar system has been confirmed by Galileo measurements (Baguhl *et al.* 1995a).

From the analysis of impact rates, impact directions, and impact speeds, our group found that the interstellar dust flow is, within the measurement uncertainties, aligned with the flow of interstellar gas through the heliosphere (Witte *et al.* 1993). Observed dust speeds from 16 to 45 km/sec are compatible with the 26 km/sec unperturbed gas speed. The mass distribution of interstellar meteoroids observed with the Ulysses dust detectors is shown in Fig. 12c. About 60% of the interstellar grains have masses between  $10^{-14}$  and  $10^{-12}$  g. The cutoff at small particle masses is real since the instruments can detect particles with a factor of 10 smaller masses. The lack of small interstellar grains in the planetary system has been suggested to be due to the effect of the interplanetary magnetic field (Grün *et al.* 1994). The mass range observed includes grains with large  $\beta$  values which, for absorbing materials, can be well above 1. However, particles with  $\beta$  values greater than 1.5 will not reach 1 AU but are deflected away from the Sun by the dominating radiation pressure force. At  $\beta < 1$  the interstellar dust flow direction as seen by Ulysses never deviates by more than  $30^\circ$  from the dust flow direction at large heliocentric distances. At  $\beta = 1$  (which we will assume here) interstellar grains pass on straight trajectories through the planetary system. The interstellar dust flux is assumed to be constant near the ecliptic plane and outside a distance that is determined by the Galileo measurements (about 2.8 AU, Baguhl *et al.* 1995a). Different reduction factors have been assumed further in ranging from no reduction to factor 30 reduction at 1 AU. With these assumptions, the impact rate of interstellar dust on any surface of given orientation can be calculated.

Populations of particles on heliocentric bound orbits have been defined by the procedure described in the previous section. Divine's core population (and the corresponding orbital distribution) has been found to fit the few particles of masses  $m > 10^{-10}$  g that have been detected and that are not affected by radiation pressure. Because of the strong influence of radiation pressure on smaller particles, we have truncated the core population at  $10^{-10}$  g and dismissed all other small particle populations of Divine, namely, the eccentric, inclined, and halo populations, since the definitions of them did not include radiation pressure effects. We define three new populations of small meteoroids, with  $\beta > 0$ , on bound heliocentric orbits to fit the Galileo and Ulysses dust measurements. Although all populations are defined over the whole mass range ( $10^{-18}$  to 1 g) each population dominates in a narrow mass interval

**TABLE III**  
Eccentricity ( $f_e$ ) and Inclination ( $f_i$ ) Distributions of the Bound Dust Populations Needed to Fit Galileo and Ulysses Observations

	Asteroidal ( $10^{-3}$ g)	Core ( $10^{-5}$ g)	A <sup>a</sup> ( $10^{-11}$ g)	B ( $10^{-13}$ g)	C ( $5 \times 10^{-15}$ g)
Eccentricity					
0	0.572	0.572	1.628	0.975	0.627
0.1	2.078	2.078	1.864	0.975	0.266
0.25	1.753	1.753	1.791	0.878	0.14
0.45	1.110	1.110	0.225	0.244	0.063
0.65	0.898	0.898	0.011	0.078	0.063
0.8	0.155	0.155	0.326	0.78	1.198
0.98	0.	0.	3.016	5.384	7.678
Inclination					
$0^\circ$	2.809	2.809	1.684	0.525	0.513
$10^\circ$	2.809	2.809	2.020	2.707	1.566
$20^\circ$	1.039	1.039	1.347	1.998	2.278
$30^\circ$	0.286	0.286	0.673	0.608	1.109
$45^\circ$	0.073	0.073	0.337	0.112	0.154
$60^\circ$	0	0	0.002	0.001	0.026
$90^\circ$	0	0	0.	0.	0.001

<sup>a</sup> Below the population name the maximum of the mass distribution is given.

for which a constant  $\beta$  value has been assumed. The A population contributes significantly to the dust flux in the mass range from  $10^{-12}$  to  $10^{-10}$  g and has  $\beta = 0.3$  (Fig. 14). The B population contributes in the range from  $2 \times 10^{-14}$  to  $10^{-11}$  g and has  $\beta = 0.8$ . The distribution functions of both A and B populations are well constrained by the measurements. For completeness, we include even smaller particles on bound orbits (C population, masses  $< 10^{-12}$  g with a peak at  $5 \times 10^{-15}$  g) having  $\beta = 0.3$ ; the distribution functions of this population are only weakly constrained by the measurements.

Table III gives orbital element distributions of Divine's asteroidal and core populations and of the new model populations found by this analysis. All populations have low inclinations which peak between  $10^\circ$  and  $20^\circ$  but the inclination distributions become increasingly wider for smaller particles. The eccentricity distributions of the A, B, and C populations are bimodal. They have a peak at low eccentricities but also a major component at high eccentricities. A technical description of the model including program codes can be found in Staubach (1996b).

## 8. VERTICAL STRUCTURE OF THE INTERPLANETARY DUST CLOUD

To derive the global interplanetary dust distribution from local dust measurements and to compare data from *in situ* dust detectors with remote sensing data (visible zodiacal light and infrared thermal emission observations)

detailed modeling is required. An early application of dynamical meteoroid modeling (cf. Leinert and Grün 1990) was the interpretation of spatial dust densities obtained from zodiacal light observations in terms of distributions of orbital elements. Haug (1958) derived an integral that transforms distribution functions of orbital elements,  $D(r_1, e, i)$ , into spatial densities at any given position in space, where  $D(r_1, e, i)$  is the number of meteoroids having perihelia between  $r_1$  and  $r_1 + dr_1$ , eccentricities between  $e$  and  $e + de$ , and inclinations between  $i$  and  $i + di$ . If the distribution function is separable,  $D(r_1, e, i) = D_1(r_1) \cdot D_e(e) \cdot D_i(i)$ , then the relative spatial density  $n(\lambda)$  at latitude  $\lambda$  is only a function of  $D_i(i)$  and  $n(\lambda)$  and is given by

$$n(\lambda) = \int_{i=\lambda}^{\pi/2} \frac{D_i(i) \cdot di}{\sqrt{\sin^2 i - \sin^2 \lambda}}. \quad (8)$$

$D_i(i) = \sin i$  results in an isotropic distribution of dust:  $n(\lambda) = \text{constant}$  and, hence, the function  $p_i(i) = D_i(i)/\sin i$  describes the deviation from isotropy. The function  $p_i(i)$  has been chosen by Divine to describe the distribution of orbit inclinations. For the transformation of Divine's distribution functions into the functions used by other investigators see Matney and Kessler (1996). Figure 15 shows the latitudinal density distributions which represent zodiacal light observations,  $n(\lambda) = \exp(-2.1 \sin \lambda)$  (Leinert *et al.* 1981), infrared observations with COBE,  $n(\lambda) = \exp(-3.26 \tan^{1.02} \lambda)$  (Reach *et al.* 1995), and those derived for the A, B, and C populations (cf. Table II) and for Divine's (1993) core population. The difference between the density distributions that fit the observed zodiacal and

infrared brightnesses suggests that zodiacal dust in the inner Solar System has a wider distribution (to which the zodiacal light measurements refer) than dust outside the Earth's orbit to which COBE data refer. Divine's core population was obtained mostly from radio meteor observations. It approximates the latitudinal density function of zodiacal light observations for low latitudes ( $\lambda < 10^\circ$ ) and that of infrared observations for high latitudes ( $\lambda > 20^\circ$ ). The density distributions for the small particle populations A, B, and C have a wider latitudinal distribution and are closer to the zodiacal light distribution. The assumed constant density of interstellar dust provides equal contributions at all latitudes.

From our dust populations, we have calculated model intensities of the zodiacal light as observed from Earth at  $90^\circ$  solar elongation. The result is shown in Fig. 16. It can be seen that by far the largest contribution comes from the core population with masses greater than  $10^{-10}$  g. Only at latitudes below  $10^\circ$  is another contribution required; this is provided by Divine's asteroidal population. Particle populations with masses  $m < 10^{-10}$  g contribute less than 1% to the zodiacal light brightness at 1 AU. To obtain this result we assumed, in accordance with Divine (1993), visual geometric albedo  $p = 0.05$  for the core population and  $p = 0.02$  for the asteroidal population. The sum of both contributions already acceptably fits the observations; therefore, we had to assume a very low albedo of  $p = 0.01$  for the small particle populations, A, B, and C. However, since we do not have independent information on the particle albedo other combinations of albedo values may provide similar good fits.

## 9. DISCUSSION

Galileo and Ulysses dust measurements directly show two dominant components of dust in interplanetary space: large interplanetary micrometeoroids on bound orbits with a wide and flat mass distribution and interstellar grains. The first component gives rise to strong variations of the impact rate observed by Galileo (Fig. 5) and to the big particle flux during Ulysses' ecliptic plane crossing (Fig. 11). The observed impact rate ( $10^{-5} \text{ sec}^{-1}$ ) during Ulysses' ecliptic plane crossing was about the same as Galileo's at the same distance despite Ulysses' higher speed (factor 2). These observations are only mutually compatible if the interplanetary component has a narrow latitudinal extent and a flat size distribution. Outside  $\pm 25^\circ$  latitude, the impact rate was down by a factor of 2 which suggests that interplanetary dust contributes only little to the flux observed at higher latitudes.

Measurements of the interstellar dust flux show a narrow size distribution, a small particle cutoff, and a limited range of trajectory directions. From Galileo measurements Baguhl *et al.* (1995a) concluded that interstellar dust can

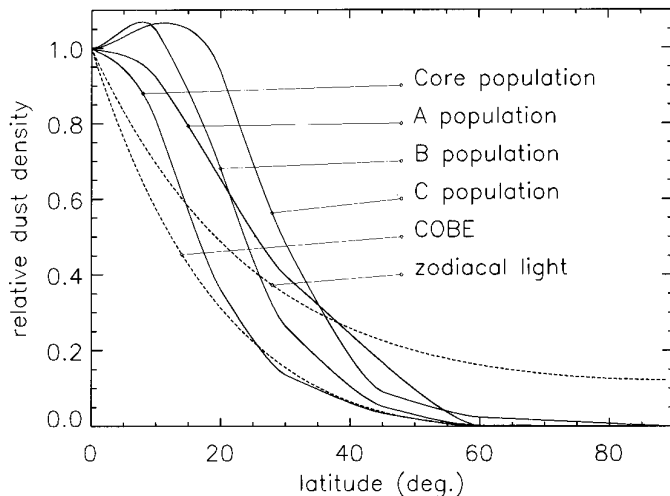


FIG. 15. Out-of-ecliptic variation of the spatial dust density. Densities derived from zodiacal light observations (Leinert *et al.* 1981) and COBE infrared observations (Reach *et al.* 1995). All densities are normalized at latitude  $l = 0^\circ$  and are compared with the density calculated for the different meteoroid populations.

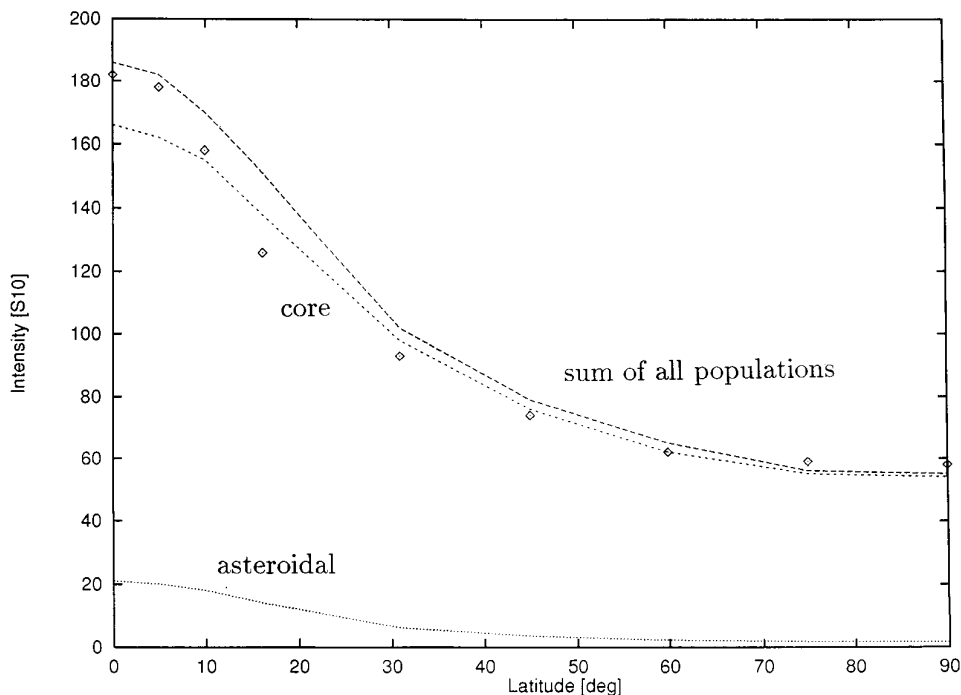


FIG. 16. Observed brightness of zodiacal light (triangles, Lévassour-Regourd and Dumont 1980) as a function latitude are compared with brightnesses of the model populations. Assumed visual geometric albedo:  $p = 0.05$  for the truncated core population,  $p = 0.02$  for the asteroidal population, and  $p = 0.01$  for the A, B, and C populations. With these albedo values, the A, B, and C populations contribute less than 1% to the brightness of the zodiacal cloud.

be reliably distinguished from interplanetary dust outside about 2.8 AU and that there the interstellar dust flux is constant, independent of heliocentric distance. On its orbit from Jupiter (5.4 AU) to the south ecliptic pole (at 2.1 AU) Ulysses measured a slowly varying flux of interstellar dust (Baguhl *et al.* 1995b), the variations being due mostly to varying detection geometry. From the measurements presented here we conclude that within the statistical and measurement limitations, no reduction of the interstellar particle flux and/or particle size has been found by Ulysses at latitudes above  $50^\circ$  and outside 1.8 AU heliocentric distance, where the contribution from interplanetary dust is considered to be insignificant.

Since interstellar dust has been uniquely identified in the outer planetary system with a roughly constant flux we assumed various depletion factors inside that region ranging from no depletion to strong depletion (factor 30) at 1 AU. A result of the model iterations is that all data sets can be matched only if we assume no reduction of the interstellar dust flux at least down to 1.3 AU where Ulysses crossed the ecliptic plane. Our model suggests that a significant reduction of the interstellar dust flux would raise the interplanetary model flux at Ulysses' ecliptic plane crossing further above the observed values (cf. Divine's model which does not include an interstellar population)

which worsens our fit. This is because meteoroids on elliptic orbits contribute to the spatial density at different heliocentric distances, and hence an increase by 30% at 1.3 AU would give rise to a comparable further increase which is in conflict also with the Galileo measurements there. Although our model does not prove it, we favor the assumption that there is little depletion of interstellar dust inside 1.8 AU from the flux level observed at 5 AU, and hence a constant interstellar flux is assumed over the whole range of the combined Galileo and Ulysses data set, i.e., from 5.4 to 0.7 AU.

In Fig. 5, individual model contributions from the interstellar and interplanetary dust populations are compared with the Galileo flux measurements. Until the second Earth flyby interstellar dust contributes between 0 and 30% to the model flux; later in the mission this contribution increases to almost 100%. Modeling results of impact rates during the Ulysses south-north passage are shown in Fig. 9. We display the contributions to the observed total flux of the interstellar dust population and the combined interplanetary dust populations. Variations in the interstellar flux are due to different sensor attitudes with respect to the interstellar dust direction. The best fit of both model fluxes is shown. Taking into account only bound heliocentric orbits (Divine 1993, dashed line),

the impact rates predicted by such a model are higher during Ulysses' ecliptic crossing and significantly lower over the solar poles.

We now compare model impact rates from different directions with those measured by Galileo and Ulysses. Figure 17a shows the same data from Galileo as Fig. 6, but this time corrected for missing impacts and binned into a  $4 \times 8$  grid in the rotation angle–time plane with impact rates represented by a gray scale. These measured impact rates are now compared with model calculations. The total model impact rate (Fig. 17b) matches the general features of the measurements quite well. The individual contributions to the directional rates show the angular separation of the interstellar population (Fig. 17c) from the interplanetary population (Fig. 17d) for most of the time.

Figure 18a shows the same data from Ulysses as in Fig. 10 except that the densities of points (i.e., fluxes) in  $4 \times 5$  segments of the diagram are represented by a gray scale. In Figs. 18b–d we show the directional characteristics of the model populations, both the combined and the individual fluxes. The agreement between the general features of the measurements and the model is satisfactory.

Since the meteoroid flux as a function of particle mass at 1 AU is well defined by many previous measurements, we want to make sure that the model results that we obtained are compatible with the flux measurements at 1 AU (Grün *et al.* 1985). Fig. 19 shows the sum of the different bound populations (solid line) and the measurement of the 1-AU dust flux. Taking into account the population of interstellar meteoroids, which contribute mostly between  $10^{-14}$  and  $10^{-10}$  g, that are not included in this figure, the conformity between both values is demonstrated.

Now we compare our results with Divine's (1993) five populations of meteoroids. The measurements considered here do not contribute significantly to our knowledge of the meteoroid flux at masses greater than  $10^{-10}$  g; therefore, we leave Divine's "asteroidal" and "core" populations for masses greater than  $10^{-10}$  g unaltered. Since particle sizes that contribute most to the zodiacal light range from 10 to  $100 \mu\text{m}$  (i.e., about  $10^{-9}$  to  $10^{-6}$  g, see Grün *et al.* 1985), there will be only a little effect of the new populations on zodiacal light models. The same holds true for radio meteors that correspond to even bigger meteoroids (Southworth and Sekanina, 1973, see also Taylor 1995). Nevertheless,

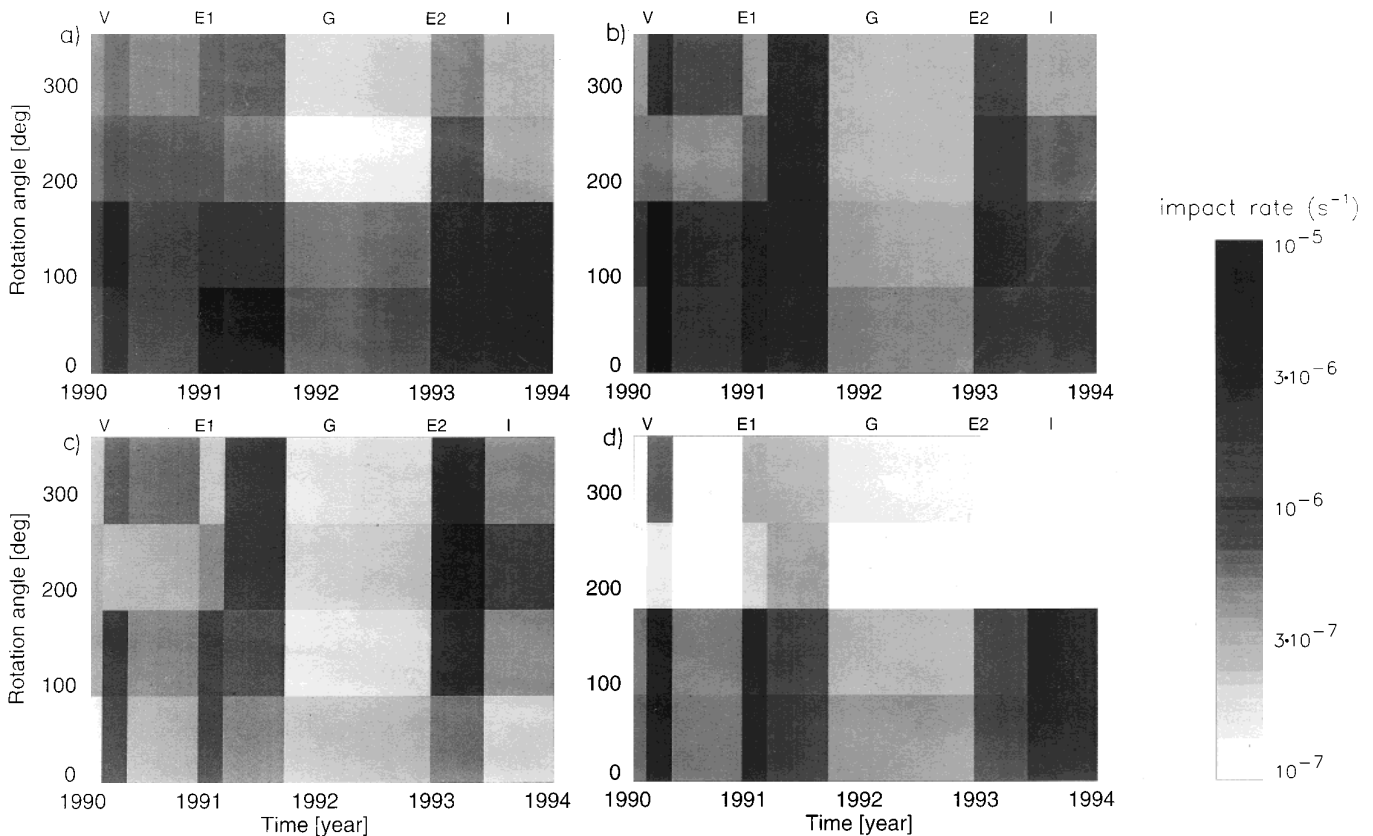


**FIG. 17.** Directional impact rates for Galileo represented by a gray scale. Observed rates (a, cf. Fig. 6) are compared with model impact rates for Galileo's initial trajectory. (b) Sum of all contributions. (c) Bound interplanetary dust. (d) Interstellar dust populations.

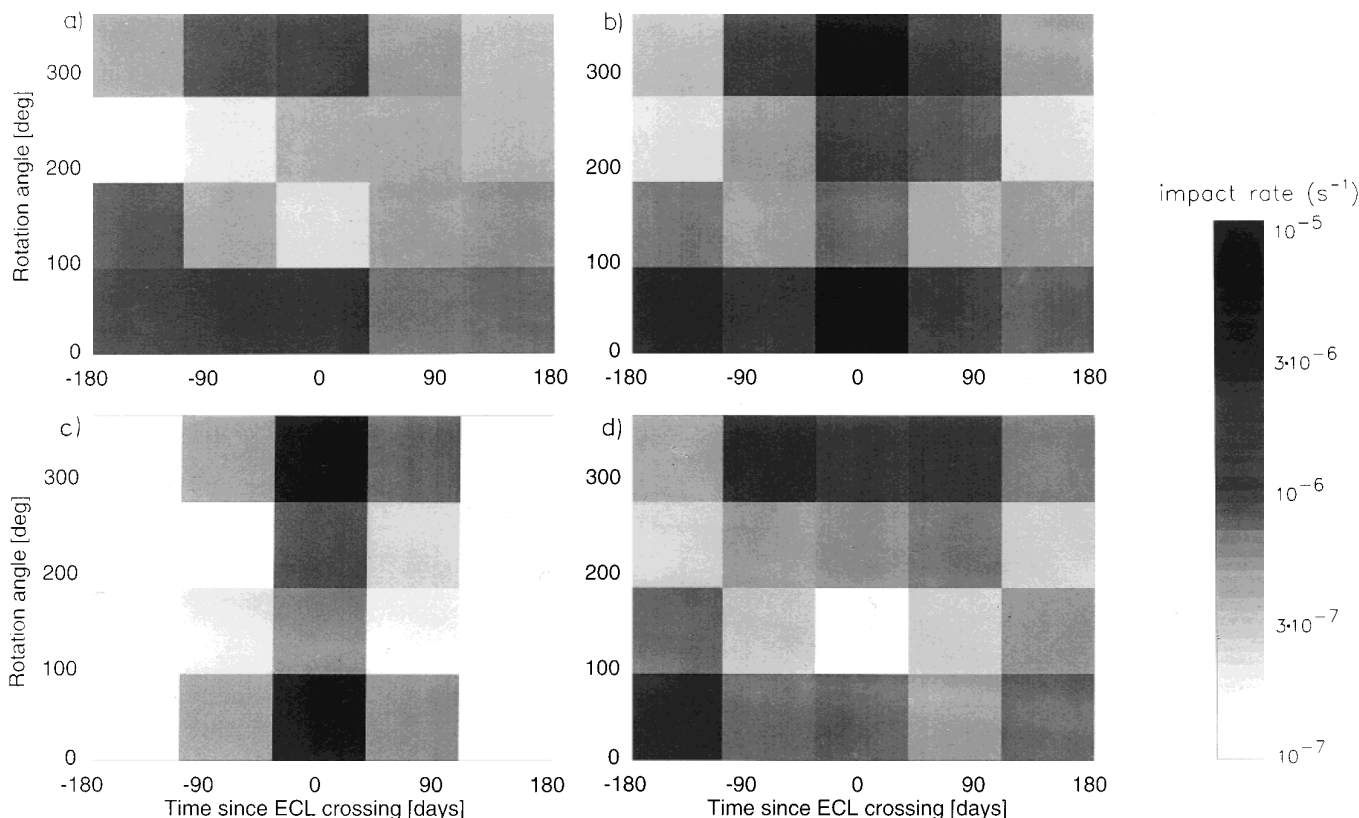


**FIG. 18.** Directional impact rates for Ulysses represented by a gray scale. Observed rates (a, cf. Fig. 10) are compared with model impact rates during Ulysses’ south–north traverse through the ecliptic plane. (b) Sum of both contributions. (c) Bound interplanetary dust. (d) Interstellar dust populations.

the core and asteroidal populations of big particles and the new bound populations are linked by a common origin. The A, B, and C populations can be regarded as the extension of the core population to small particles for which radiation pressure is important.

There are significant differences between our new dust populations and the three small particle populations defined by Divine (1993). No “inclined,” “eccentric,” and “halo” populations are needed to explain the Galileo and Ulysses data sets. However, some of these populations may be required to model data (Pioneer 10, and 11 and Helios) which we did not consider here. Therefore, Divine’s small particle populations must have a more restricted validity range not to disturb the match of our new populations with the Galileo and Ulysses data. For example, the “halo” population may still be needed for masses above  $10^{-9}$  g to describe the Pioneer 10 and 11 fluxes which were observed to arrive from the direction opposite the interstellar flux. The “inclined” population may still be needed in the inner Solar System ( $<0.7$  AU) to explain some of the Helios data, although some of that may already be described by the new interstellar, A, B, and C populations.

$\beta$ -Meteoroids, which are particles that leave the Solar System on hyperbolic orbits because of radiation pressure and electromagnetic solar wind interactions, could not be observed by Galileo and Ulysses because of geometric viewing constraints except for a few short periods during the Ulysses mission: the early mission phase, both polar passes, and the ecliptic plane crossing.  $\beta$ -Meteoroids with a significant outward velocity component were not observable at all by Galileo. They also would have made only small contributions to the data set of large particles discussed here because of our cutoff in considered impact charges ( $8 \times 10^{-14}$  C). However, the high-eccentricity component of the small A, B, and C populations may be extensions of such a new hyperbolic  $\beta$ -meteoroid population. Further work is needed, especially a compilation of observations of  $\beta$ -meteoroids and improved modeling of this population.

## 10. SUMMARY AND CONCLUSION

Dust in the planetary system has been observed by two identical dust detectors on board the Galileo and Ulysses

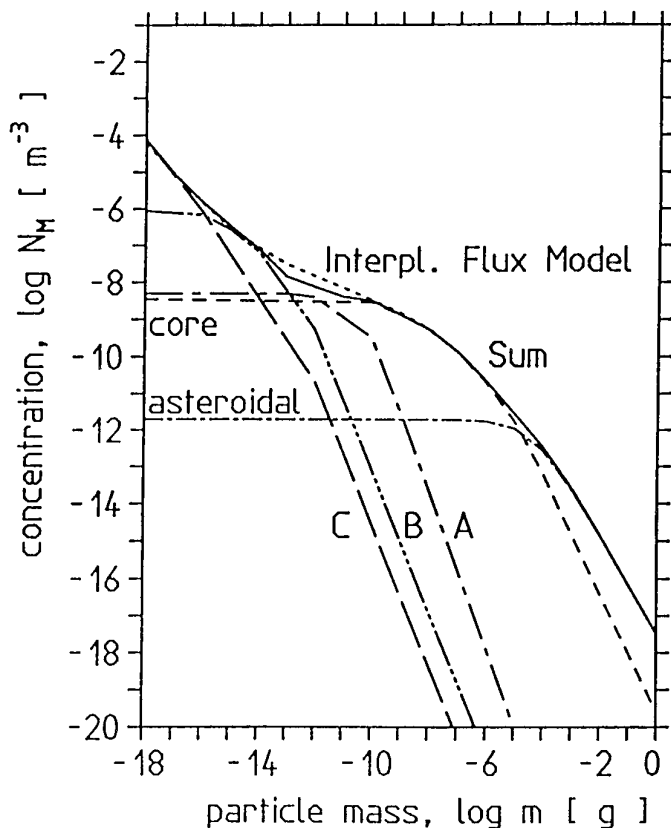


FIG. 19. Measurements of the meteoroid flux at 1 AU (short dashes, Interplanetary Flux Model from Grün *et al.* 1985) and the contributions from the different bound populations. The sum of the bound populations is shown by the solid line; no interstellar dust flux is included.

space probes. Measurements have been taken in the ecliptic plane over a wide range of heliocentric distances and from an orbit almost perpendicular to the ecliptic plane. Radial profiles of the dust flux have been obtained by Galileo from 0.7 to 5.4 AU in the ecliptic plane and a latitudinal profile has been obtained by Ulysses from  $-79^\circ$  to  $+79^\circ$  ecliptic latitude. In the inner Solar System strong variations of the interplanetary dust flux were observed as function of spacecraft position and direction of spacecraft motion. Outside 3 AU and at high latitudes a roughly constant monodirectional flux of interstellar dust caused most of the impacts observed.

Two distinct major dust components are recognized in both data sets: (1) inside 3 AU interplanetary dust has been observed with a flat mass distribution (masses ranged from  $10^{-16}$  to  $10^{-6}$  g) on low to moderate eccentric orbits and with a narrow latitudinal distribution, and (2) a monodirectional flux of interstellar dust has been positively identified outside (1.8 AU from the Sun with a narrow mass distribution ( $10^{-14}$  to  $10^{-12}$  g). Inside 1.8 AU interstellar

dust was not uniquely identifiable among the dominant interplanetary dust component.

For quantitative analysis of these data we follow Divine's (1993) modeling technique that fits meteoroid measurements with different populations of interplanetary meteoroids. Each population is defined by a distinct set of orbital elements and a size distribution. We have extended this model (1) by considering the effect of radiation pressure on small particles, (2) by including a particle population on hyperbolic orbits, and (3) by modeling directional and speed information together with impact rates.

Galileo and Ulysses dust data are fit by four interplanetary dust populations on bound orbits and an interstellar dust population on hyperbolic trajectories. Particles with masses greater than  $10^{-10}$  g move on low to moderate eccentric orbits and have low inclinations. Three populations of smaller dust particles (from  $10^{-10}$  g to  $10^{-16}$  g) are affected by radiation pressure. Their orbital element distributions resemble the bigger particle population except that they contain a high-eccentricity component and they have wider latitudinal distributions. The similarities of their orbits suggest that all four populations on bound orbits may be genetically related and that they are part of a larger meteoroid complex. The interstellar dust population has been modeled by a flux of small particles that arrive from about  $250^\circ$  ecliptic longitude at a speed of 26 km/sec with  $\beta = 1$ .  $\beta$ -Meteoroids leaving the Solar System on hyperbolic orbits have been neglected in this analysis because they do not contribute significantly to the Galileo and Ulysses data sets considered here. The model is compatible with the size distribution measured at 1 AU and with zodiacal light observations.

The existence of interstellar dust inside 2 AU has consequences for the material properties of the observed grains: (1) the radiation pressure constant,  $\beta$ , of these particles cannot exceed 1 by far (i.e., the particles cannot consist out of highly absorbing material like pure carbon or be very fluffy; both properties would give rise to higher  $\beta$  values), and (2) no volatile material like water ice is stable at these distances (therefore, the observed interstellar grains can be composed only of refractory materials, potentially including some semivolatile carbonaceous material). Sublimation of the carbonaceous component of interstellar grains near the Sun could explain carbon pickup ions of interstellar origin which have been found by the Ulysses SWICS instrument (Geiss *et al.* 1996). Detection of interstellar dust close to the Earth's orbit opens the door for detailed *in situ* analysis of this relatively unknown material. Next steps toward this important goal are expected from the Cassini and Stardust missions.

#### ACKNOWLEDGMENTS

We thank the Galileo and Ulysses operations teams for their effective cooperation in acquiring the data on which this research is based. We

are grateful to the late Neil Divine for his support and encouragement during the development of the extended meteoroid model. Discussions with Walter Flury and Rüdiger Jehn, from ESOC, were instrumental for the implementation of the new meteoroid model. We thank Bill Reach for his considered suggestions which improved the paper significantly. Support from DARA and ESOC is acknowledged.

## REFERENCES

- Baguhl, M., E. Grün, G. Linkert, D. Linkert, and N. Siddique 1993. Identification of 'small' dust impacts in the Ulysses dust detector data. *Planet. Space Sci.* **41**, 1085–1098.
- Baguhl, M., E. Grün, D. P. Hamilton, G. Linkert, and P. Staubach 1995a. The flux of interstellar dust observed by Ulysses and Galileo. *Space Sci. Rev.* **72**, 471–476.
- Baguhl, M., D. P. Hamilton, E. Grün, S. F. Dermott, H. Fechtig, M. S. Hanner, J. Kissel, B. A. Lindblad, D. Linkert, G. Linkert, I. Mann, J. A. M. McDonnell, G. E. Morfill, C. Polanskey, R. Riemann, G. Schwehm, P. Staubach, and H. A. Zook 1995b. Dust measurements at high ecliptic latitudes. *Science* **268**, 1016–1019.
- Burns, J. A., P. L. Lamy, and S. Soter 1979. Radiation forces on small particles in the Solar System. *Icarus* **40**, 1–48.
- Dermott, S. F., S. Jayarama, Y. L. Xu, B. A. S. Gustafson, and J. C. Liou 1994. A circumsolar ring of asteroidal dust in resonant lock with the Earth. *Nature* **369**, 719–723.
- Divine, N. 1993. Five populations of interplanetary meteoroids. *J. Geophys. Res.* **98**, 17029–17048.
- Draine B. T., and H. M. Lee 1984. Optical properties of interstellar graphite and silicate grains. *Astrophys. J.* **285**, 89–108.
- Dumont, R., and A. C. Levasseur-Regourd 1985. Zodiacal light gathered along the line of sight. Retrieval of the local scattering coefficient from photometric surveys of the ecliptic plane. *Planet. Space Sci.* **33**, 1–9.
- Geiss, J., G. Gloeckler, L. A. Fisk, and R. V. Steiger 1996. C<sup>+</sup> pick-up ions in the heliosphere and their origin. *J. Geophys. Res.* **100**, 23373–23377.
- Giese, R. H., B. Kneissel, and U. Rittich 1986. Three-dimensional models of the zodiacal dust cloud: A comparative study. *Icarus* **68**, 395–411.
- Grün, E., M. Baguhl, N. Divine, H. Fechtig, D. P. Hamilton, M. S. Hanner, J. Kissel, B. A. Lindblad, D. Linkert, G. Linkert, I. Mann, J. A. M. McDonnell, G. E. Morfill, C. Polanskey, R. Riemann, G. Schwehm, N. Siddique, P. Staubach, and H. A. Zook, 1995a. Three years of Galileo dust data. *Planet. Space Sci.* **43**, 971–999.
- Grün, E., M. Baguhl, N. Divine, H. Fechtig, D. P. Hamilton, M. S. Hanner, J. Kissel, B. A. Lindblad, D. Linkert, G. Linkert, I. Mann, J. A. M. McDonnell, G. E. Morfill, C. Polanskey, R. Riemann, G. Schwehm, N. Siddique, P. Staubach, and H. A. Zook, 1995b. Two years of Ulysses dust data. *Planet. Space Sci.* **43**, 971–999.
- Grün, E., M. Baguhl, H. Fechtig, M. S. Hanner, J. Kissel, B. A. Lindblad, D. Linkert, G. Linkert, J. A. M. McDonnell, G. E. Morfill, G. Schwehm, N. Siddique, and H. A. Zook, 1992a. Interplanetary dust measurement by the Galileo and Ulysses dust detectors during the initial mission phases. In *Hypervelocity Impacts in Space* (J. A. M. McDonnell, Ed.), pp. 173–179. Univ. of Kent, Canterbury.
- Grün, E., M. Baguhl, D. P. Hamilton, J. Kissel, D. Linkert, G. Linkert, and R. Riemann, 1995c. Reduction of Galileo and Ulysses dust data. *Planet. Space Sci.* **43**, 941–951.
- Grün, E., M. Baguhl, D. P. Hamilton, R. Riemann, H. A. Zook, S. Dermott, H. Fechtig, B. A. Gustafson, M. S. Hanner, M. Horanyi, K. K. Khurana, J. Kissel, M. Kivelson, B. A. Lindblad, D. Linkert, G. Linkert, I. Mann, J. A. M. McDonnell, G. E. Morfill, C. Polanskey, G. Schwehm, and R. Srama 1996. Constraints from Galileo observations on the origin of jovian dust streams. *Nature* **381**, 395–398.
- Grün, E., H. Fechtig, R. H. Giese, J. Kissel, D. Linkert, D. Maas, J. A. M. McDonnell, G. E. Morfill, G. Schwehm, and H. A. Zook, 1992b. The Ulysses dust experiment. *Astron. Astrophys. Suppl.* **92**, 411–423.
- Grün, E., H. Fechtig, M. S. Hanner, J. Kissel, B. A. Lindblad, D. Linkert, G. E. Morfill, and H. A. Zook, 1992c. The Galileo dust detector. *Space Sci. Rev.* **60**, 317–340.
- Grün, E., B. Gustafson, I. Mann, M. Baguhl, G. E. Morfill, P. Staubach, A. Taylor, and H. A. Zook 1994. Interstellar dust in the heliosphere. *Astron. Astrophys.* **286**, 915–924.
- Grün, E., H. A. Zook, M. Baguhl, A. Balogh, S. J. Bame, H. Fechtig, R. Forsyth, M. S. Hanner, M. Horanyi, J. Kissel, B.-A. Lindblad, D. Linkert, G. Linkert, I. Mann, J. A. M. McDonnell, G. E. Morfill, J. L. Phillips, C. Polanskey, G. Schwehm, N. Siddique, P. Staubach, J. Svestka, and A. Taylor 1993. Discovery of jovian dust streams and interstellar grains by the Ulysses spacecraft. *Nature* **362**, 428–430.
- Grün, E., H. A. Zook, H. Fechtig, and R. H. Giese 1985. Collisional balance of the meteoritic complex. *Icarus* **62**, 244–272.
- Gustafson, B. A. S. 1994. Physics of zodiacal dust. *Annu. Rev. Earth. Planet. Sci.* **22**, 553–595.
- Gustafson, B. A. S., and N. Y. Misconi 1979. Streaming of interstellar grains in the Solar System. *Nature* **282**, 276–278.
- Hamilton, D. P., and J. A. Burns 1992. Stability zones about asteroids. II. The destabilizing effects of eccentric orbits and of solar radiation. *Icarus* **96**, 43–64.
- Hamilton, D. P., E. Grün, and M. Baguhl 1996. Electromagnetic escape of dust from the Solar System. In *Physics, Chemistry and Dynamics of Interplanetary Dust* (B. A. S. Gustafson and M. S. Hanner), ASP Conference Series, Astronomical Society of the Pacific, San Francisco. No. 104, pp. 31–34.
- Hanner M. S., J. G. Sparrow, J. L. Weinberg, and D. E. Beeson 1976. Pioneer 10 observations of zodiacal light brightness near the ecliptic: Changes with heliocentric distance. In *Interplanetary Dust and Zodiacal Light* (H. Elsaesser and H. Fechtig, Eds.), Lecture Notes in Physics, 48, pp. 29–35. Springer-Verlag, Heidelberg.
- Haug, U. 1958. Über die Häufigkeitsverteilung der Bahnelemente bei den interplanetaren Staubeilchen. *Z. Astrophys.* **44**, 71–97.
- Hauser, M. G., F. C. Gillett, F. J. Low, T. N. Gautier, C. A. Beichman, G. Neugebauer, H. H. Aumann, B. Baud, N. Boogess, J. P. Emerson, J. R. Houck, B. T. Soiffer, and R. G. Walker 1984. IRAS observations of the diffuse infrared background. *Astrophys. J.* **278**, L15–L18.
- Johnson, T. V., C. M. Yeates, and R. Young 1992. Galileo mission overview. *Space Sci. Rev.* **60**, 3–21.
- Leinert, C., and E. Grün 1990. Interplanetary dust. In *Physics and Chemistry in Space* (R. Schwenn and E. Marsch, Eds.), pp. 207–275. Springer-Verlag, Heidelberg.
- Leinert, C., H. Link, and E. Pitz 1976. Interpretation of a rocket photometry of the inner zodiacal light. *Astron. Astrophys.* **47**, 221–230.
- Leinert, C., I. Richter, E. Pitz, and B. Planck 1981. The zodiacal light from 1.0 to 0.3 AU as observed by the Helios space probes. *Astron. Astrophys.* **103**, 177–188.
- Levasseur-Regourd, A. C., and R. Dumont 1980. Absolute photometry of zodiacal light. *Astron. Astrophys.* **84**, 277–279.
- Mann, I., E. Grün, and M. Wilk 1996. The contribution of asteroid dust to the interplanetary dust cloud: The impact of Ulysses results on the understanding of the IRAS dust bands. *Icarus* **120**, 399–407.
- Matney, M. J., and D. J. Kessler 1996. A revision of Divine's interplanetary meteoroid model. In *Physics, Chemistry and Dynamics of Interplanetary Dust* (B. A. S. Gustafson and M. S. Hanner, Eds.), ASP Conference Series, No. 104, pp. 15–18.
- Morfill, G. E., and E. Grün 1979. The motion of charged dust particles

- in interplanetary space. II. Interstellar grains. *Planet. Space Sci.* **27**, 1283–1292.
- Reach, W. T., B. A. Franz, J. L. Weiland, M. G. Hauser, T. N. Kelsall, E. L. Wright, G. Rawley, S. W. Stemwedel, and W. J. Spiesman 1995. Observational confirmation of a circumsolar dust ring by the COBE satellite. *Nature* **374**, 521–523.
- Southworth, R. B., and Z. Sekanina 1973. *Physical and Dynamical Studies of Meteors*. NASA CR-2316.
- Staubach P. 1996a. *Numerische Modellierung der Dynamik von Mikrometeoroiden und ihre Bedeutung für interplanetare Raumsonden und geozentrische Satelliten*. Ph.D. thesis, Univ. of Heidelberg.
- Staubach, P. 1996b. *Upgrade of the DISCOS Meteoroid Model*. Final Report, ESOC Contract 10463/93/D/CS, ESOC, Darmstadt.
- Staubach, P., N. Divine, and E. Grün 1993. Temperatures of zodiacal dust. *Planet. Space Sci.* **41**, 1099–1108.
- Staubach, P., E. Grün, and R. Jehn 1996. The meteoroid environment near Earth. *Adv. Space Res.*, in press.
- Taylor, A. D. 1995. The Harvard Radio Meteor Project meteor velocity distribution reappraised. *Icarus* **116**, 154–158.
- Wenzel, K. P., R. G. Marsden, D. E. Page, and E. J. Smith 1992. The Ulysses mission. *Astron. Astrophys. Suppl.* **92**, 207–219.
- Witte, M., H. Rosenbauer, M. Banaszekiewicz, and H. Fahr 1993. The Ulysses neutral gas experiment: Determination of the velocity and temperature of the interstellar neutral helium. *Adv. Space Res.* **13**, (6)121–(6)130.